

PERFORMANCE CHARACTERIZATION OF COMPLEX FUEL PORT  
GEOMETRIES FOR HYBRID ROCKET FUEL GRAINS

by

Andrew Bath

A thesis submitted in partial fulfillment  
of the requirements for the degree

of

MASTER OF SCIENCE

in

Mechanical Engineering

Approved:

---

Stephen A. Whitmore  
Major Professor

---

David Geller  
Committee Member

---

R. Rees Fullmer  
Committee Member

---

Charles M. Swenson  
Committee Member

---

Mark R. McLellan  
Vice President for Research and  
Dean of the School of Graduate Studies

UTAH STATE UNIVERSITY  
Logan, Utah

2012

Copyright © Andrew Bath 2012

All Rights Reserved

## Abstract

Performance Characterization of Complex Fuel Port Geometries for Hybrid Rocket Fuel  
Grains

by

Andrew Bath, Master of Science

Utah State University, 2012

Major Professor: Stephen A. Whitmore

Department: Mechanical and Aerospace Engineering

This research investigated the 3D printing and burning of fuel grains with complex geometry and the development of software capable of modeling and predicting the regression of a cross-section of these complex fuel grains. The software developed did predict the geometry to a fair degree of accuracy, especially when enhanced corner rounding was turned on. The model does have some drawbacks, notably being relatively slow, and does not perfectly predict the regression. If corner rounding is turned off, however, the model does become much faster; although less accurate, this method does still predict a relatively accurate resulting burn geometry, and is fast enough to be used for performance-tuning or genetic algorithms. In addition to the modeling method, preliminary investigations into the burning behavior of fuel grains with a helical flow path were performed. The helix fuel grains have a regression rate of nearly 3 times that of any other fuel grain geometry, primarily due to the enhancement of the friction coefficient between the flow and flow path.

(67 pages)

## Public Abstract

Performance Characterization of Complex Fuel Port Geometries for Hybrid Rocket Fuel  
Grains

by

Andrew Bath, Master of Science

Utah State University, 2012

Major Professor: Stephen A. Whitmore  
Department: Mechanical and Aerospace Engineering

Extensive research in hybrid rocket motors has taken place at the department of Mechanical and Aerospace Engineering at USU (Utah State University) in the last several years. USU has one of the few facilities in the country capable of static-test firing rocket motors on-campus, which allows for fast-paced testing and development not available elsewhere. Research has involved investigating propulsion devices for a range of applications, including micro-satellite thrusters, hot-gas generators, and even jet-assisted takeoff kick motors. Hybrid motors have the advantage of safety over any other chemical propulsion. Since the fuel and oxidizer are stored separately, they are relatively inert until combined in a hot-gas environment, making them ideal for applications where safety is a major concern, such as a secondary or tertiary payload for a major rocket launch. Development of this technology has been slow, as poorly-designed hybrid rocket motors are not competitive with other chemical propulsion technologies, but recent advances made at USU and other universities are beginning to show that hybrids do have a place in the market.

Hybrid research at USU has been ongoing for several years, with a budget of around \$500,000 over the last three years. Most of this money has funded instrumentation and manufacturing materials, as well as financial support for the graduate student research team.

This funding has come from multiple sources, including the Space Dynamics Lab (SDL), the State of Utah, and NASA. Many technical papers have been presented at technical conferences and published in peer-reviewed journals, with more on the way.

Part of the research into hybrid rockets involves 3D printing hybrid fuel grains to obtain complex geometries inside the motor to improve performance. This capability has given rise to the need to be able to model the geometric regression of these complex fuel grain structures as they burn. This model must be easy to develop for any fuel grain geometry, with the ability to model anything that is printable. Current methods of geometric regression are either custom-designed for each geometry, or are slow and unstable mathematical simulations. An alternative method proposed is to use image processing methods to regress a fuel grain. This means all that is required to model the burnback of fuel grain geometry is a picture of a cross-section of the fuel grain, which is trivial to obtain from a CAD file or other sources. This research will be an enabling technology for modeling new types of fuel grains that increase the performance of hybrid rocket motors, allowing them to have more competitive performance against other chemical propulsion technologies.

# Contents

|   | Page        |
|---|-------------|
| <b>Abstract</b> . . . . .   | <b>iii</b>  |
| <b>Public Abstract</b> . . . . .                                      | <b>iv</b>   |
| <b>List of Tables</b> . . . . .                                       | <b>vii</b>  |
| <b>List of Figures</b> . . . . .                                      | <b>viii</b> |
| <b>Nomenclature</b> . . . . .   | <b>x</b>    |
| <b>1 Introduction</b> . . . . .                                       | <b>1</b>    |
| <b>2 Background on Hybrid Rockets</b> . . . . .                       | <b>4</b>    |
| 2.1 Advantages of Hybrid Rocket Systems . . . . .                     | 5           |
| 2.2 Technical Limitations of Hybrid Rocket Systems . . . . .          | 5           |
| 2.3 Hybrid Design and Fabrication Methods . . . . .                   | 6           |
| <b>3 Literature Survey</b> . . . . .                                  | <b>9</b>    |
| <b>4 Regression Modeling</b> . . . . .                                | <b>12</b>   |
| 4.1 Solid Propellant Fuel Grain Regression Modeling . . . . .         | 12          |
| 4.2 Two-Dimensional Hybrid Fuel Grain Modeling . . . . .              | 14          |
| 4.3 Three-Dimensional Hybrid Fuel Grain Regression Modeling . . . . . | 19          |
| <b>5 Research Objectives</b> . . . . .                                | <b>25</b>   |
| <b>6 Geometric Regression Model Development</b> . . . . .             | <b>28</b>   |
| 6.1 Geometric Regression Algorithm . . . . .                          | 28          |
| <b>7 Results</b> . . . . .  | <b>33</b>   |
| 7.1 Motor Testing . . . . .   | 33          |
| 7.2 Threshold Characterization . . . . .                              | 37          |
| 7.3 Geometric Results Comparison . . . . .                            | 39          |
| 7.4 Thrust Comparison . . . . .                                       | 42          |
| 7.5 Helix Results . . . . .   | 44          |
| 7.6 Data Table . . . . .  | 50          |
| <b>8 Summary and Conclusion</b> . . . . .                             | <b>52</b>   |
| <b>References</b> . . . . .   | <b>53</b>   |

## List of Tables

| Table  | Page |
|--|------|
| 2.1 Comparison of chemical rocket motor characteristics. . . . .     | 5    |
| 4.1 Saint Robert's curve fits for various solid propellants. . . . . | 13   |
| 5.1 Previous burn geometries to be analyzed. . . . .                 | 26   |
| 5.2 New burn geometries to be analyzed. . . . .                      | 27   |
| 7.1 Test plan matrix. . . . .  | 51   |

## List of Figures

| Figure   | Page |
|--|------|
| 3.1 Hybrid wagon-wheel fuel grain. . . . .   | 11   |
| 4.1 Linear fuel port regression. . . . .   | 12   |
| 4.2 Solid propellant grain port geometries and corresponding burn thrust profiles.         | 14   |
| 4.3 Longitudinal boundary layer development within the fuel port. . . . .                  | 18   |
| 4.4 Burned HTPB and ABS fuel grains. . . . .   | 18   |
| 4.5 Predicted and measured linear regression for HTPB and ABS grains. [1] . .              | 19   |
| 4.6 Geometric regression via blurring. . . . .   | 21   |
| 4.7 Arbitrary grain geometry regressed $3 \frac{\text{pixel}}{\text{iteration}}$ . . . . . | 22   |
| 4.8 Fast marching algorithm example [2] . . . . .  | 23   |
| 6.1 Example fuel grain regressed with zero threshold . . . . .                             | 30   |
| 6.2 Basic disk filter example . . . . .  | 30   |
| 6.3 Disk filter fit curve . . . . .  | 31   |
| 6.4 Thresholding examples . . . . .  | 31   |
| 6.5 Example fuel grain regressed with a 35% threshold . . . . .                            | 32   |
| 6.6 Software algorithm block diagram. . . . .  | 32   |
| 7.1 Motor test stand with 98mm motor. . . . .  | 33   |
| 7.2 MoNSTeR cart plumbing diagram. . . . .   | 34   |
| 7.3 Assembled fuel grain diagram. . . . .  | 35   |
| 7.4 Goldfish fuel grain . . . . .  | 36   |
| 7.5 Threshold matching . . . . .   | 37   |
| 7.6 Threshold matching zoom . . . . .  | 38   |



|      |   |    |
|------|---|----|
| 7.7  | Geometric propagator with thresholding vs. hot fire results summary . . . . | 39 |
| 7.8  | Geometric propagator without thresholding vs. hot fire results summary . .  | 41 |
| 7.9  | Poor geometric propagation example . . . . .                                | 42 |
| 7.10 | Maltese cross performance comparison . . . . .                              | 43 |
| 7.11 | Goldfish grain performance comparison . . . . .                             | 44 |
| 7.12 | Helix thrust and chamber pressure . . . . .                                 | 46 |
| 7.13 | Helix fuel grain 3D scans . . . . .   | 48 |
| 7.14 | Helical, 98mm, and 75mm regression rates . . . . .                          | 49 |

## Nomenclature

|               |  |
|---------------|--|
| $a$           | Regression rate scaling factor                   |
| $A_{burn}$    | Burning surface area                             |
| $A_{chamber}$ | Chamber area                                     |
| $A_{ox}$      | Injector discharge area                          |
| $A_{port}$    | Port area  |
| $A_{burn}$    | Burning surface area                             |
| $C_{dox}$     | Injector discharge coefficient                   |
| $C_f$         | Skin friction coefficient                        |
| $dt$          | Timestep   |
| $dx$          | Horizontal image conversion factor               |
| $dy$          | Vertical image conversion factor                 |
| $A_{final}$   | Final helix surface area                         |
| $f_{cblas}$   | Blasius friction factor                          |
| $f_{cgniel}$  | Gnielinski friction factor                       |
| $G$           | Oxidizer mass flux                               |
| $H$           | Image height                                     |
| $\bar{I}$     | Image  |
| $I_{sp}$      | Specific impulse                                 |
| $m$           | Columns of $\bar{I}$                             |
| $N$           | Helical Friction Factor                          |
| $n$           | Rows of $\bar{I}$                                |
| $n_{p_x}$     | Number of pixels in the x-direction of the image |
| $n_{p_y}$     | Number of pixels in the y-direction of the image |

|                     |                                  |
|---------------------|----------------------------------|
| $P$                 | Port perimeter                   |
| $P_0$               | Chamber pressure                 |
| $P_{ox}$            | Oxidizer pressure                |
| $Pr$                | Prandtl number                   |
| $\dot{r}$           | Regression rate                  |
| $r_{final}$         | Final helix radius               |
| $r_{init}$          | Initial helix radius             |
| $T_0$               | Combustion flame temperature     |
| $T_{fuel}$          | Fuel temperature                 |
| $V_c$               | Fuel port volume                 |
| $W$                 | Image width                      |
| $\bar{X}$           | X boundary coordinates           |
| $\bar{Y}$           | Y boundary coordinates           |
| $c_p$               | Specific heat                    |
| $n$                 | Regression rate scaling exponent |
| $\dot{r}$           | Regression rate                  |
| $\rho_{propellant}$ | Propellant density               |
| $h_v$               | Heat of vaporization             |
| $\mu$               | Viscosity                        |
| $\rho_{fuel}$       | Fuel density                     |
| $\rho_{ox}$         | Oxidizer density                 |

# Chapter 1

## Introduction

Multiple fuel grains with complex embedded fuel port geometries were be fabricated and burned, and the resulting regression rates, burn profiles, and motor performance parameters were measured. These test results were be compared against existing hybrid motor performance models. To supplement these analytical comparisons, a novel method for propagating the fuel port burn surface was developed and compared with the experimental fuel burn patterns. This method models the fuel cross section as an array of gray scale pixels and image-processing techniques are used to regress the fuel grain geometry.

This work utilizes the recent capability growth in factory automation and robotics. A type of direct-digital manufacturing known as Fused Deposition Modeling (FDM) [3], commonly known as “rapid-prototyping,” was be used to fabricate hybrid rocket fuel grains with complex embedded fuel port structures. FDM manufacturing uses additive fabrication principles by depositing materials in layers to build up a structure. A thermoplastic filament is supplied to an extrusion nozzle, which heats the material to near its melting point and extruded. The nozzle is then moved in both horizontal and vertical directions by a computer numerically controlled (CNC) mechanism. This manufacturing method can support high production rates, and offers the potential to improve hybrid fuel grain quality, consistency, and performance, while reducing development and production costs.

The material most commonly used for FDM manufacturing is acrylonitrile-butadiene-styrene (ABS). ABS is an inexpensive, recyclable thermoplastic with a relatively low melting point. ABS can also be reshaped and recycled multiple times with little or no degradation of material properties. This material is widely produced for a variety of non-combustion applications including household plumbing, structural materials, and children’s toys. More than 1.4 billion kilograms of ABS material were produced by petrochemical industries worldwide

in 2010 [4].

A major result of research just recently completed by Whitmore, et al. at Utah State University (USU) [1] was the demonstrated thermodynamic equivalence of ABS to the most commonly used hybrid rocket fuel, Hydroxyl-Terminated Polybutadiene (HTPB). This research showed that when ABS is burned with nitrous oxide ( $N_2O$ ), the combustion flame temperature is slightly cooler than HTPB, but the products of combustion have a lower molecular weight. Thus ABS achieves specific impulse (Isp) and characteristic velocity ( $c^*$ ) that are nearly equivalent to HTPB. ABS and HTPB fuel regression rates were measured to be nearly identical. This similarity in burn performance allows the substitution of FDM-manufactured ABS fuel grains with little or no thermodynamic performance penalty.

When compared to HTPB, ABS has several mechanical properties that make it very attractive as a hybrid rocket fuel. As mentioned in the previous paragraphs, it is possible to embed complex, high-surface area flow paths within the fuel grain [5]. These internal flow paths can open-up during a burn and allow for motor aspect ratios that are significantly shorter than can be achieved using conventional motor-casting technologies. These embedded flow paths cannot be achieved with HTPB grains that are cast around mandrels and tooling that must be removed once the material is set.

HTPB is a legacy thermoset polymer material that is mixed from its liquid base-components, degassed under vacuum, and then cast and cured in a fuel grain mold. HTPB does not melt in the presence of heat, but instead chars and ablates. HTPB burn properties can vary dramatically depending on the curative mix ratio, relative humidity, cure temperature, degree of residual gas seeding in the cast material, and the length of time the material has cured. Typical cure times can vary from two days to two weeks. Because HTPB is a thermosetting material, it cannot be shaped and manufactured using FDM methods. Once cast the HTPB grain cannot be reshaped, reused, or recycled.

Because ABS melts before vaporizing when subjected to heat, a liquid film layer is produced along the length of the fuel port, and this film-layer has the effect of providing a significant amount of film cooling. This insulating film layer directs the heat of combustion

towards the nozzle exit, and allows the external motor case to remain cool during the burn. This self-cooling property of ABS presents a very significant advantage for in space applications where thermal management becomes a big issue.

Finally, ABS has a very high structural modulus (2.3 GPa) and tensile yield strength (40 MPa). This yield strength is approximately 38% of aluminum. In any design consideration the relative strength and insulation properties of the ABS will allow the fuel grain to take a significant portion of the combustion chamber pressure load and reduces the wall thickness requirements. Because ABS is structurally strong and self-insulating, potentially the entire combustion chamber can be fabricated of the ABS fuel material.

## Chapter 2

### Background on Hybrid Rockets

During the past 50 years conventional launch systems have been developed to a high state of capability; however, for a variety of reasons these vehicles have become increasingly expensive to operate. Some of these reasons include manufacturing and operational complexity, safety and environmental regulations for dealing with hazardous materials, and the generally large support army required for flight preparations. Because of high launch performance demands, including specific impulse ( $I_{sp}$ ) and thrust-to-weight ratio, conventional liquid and solid-propelled rocket stages that employ highly-energetic, explosive, or toxic propellants will likely remain the systems of choice for large military-class payloads or for human spaceflight. However, there exists an emerging commercial market that is willing to accept a lower system performance in exchange for reduced operational costs and lower environmental impact. Hybrid rockets, powered by safe, non-toxic propellants, have the ability to fill this growing niche market.

There are three types of chemically-propelled rockets; liquid, solid and hybrid. Liquid propellant rockets use highly volatile liquid oxidizer and liquid fuel components that are mixed and burned in the combustion chamber. Solid rocket motors use a solid propellant grain that mixes both the oxidizer and fuel in a hydrocarbon binder. Both liquid rocket engines (due to combustion instability) and solid rocket motors (due to the extreme volatility and energy levels of the combined propellants) have a potential for catastrophic failure. By contrast, hybrid rocket motors separate the oxidizer (typically benign oxidizers like nitrous oxide) and fuel (usually inert solid hydrocarbon fuel grains), and thus present little risk of explosion. This inherent safety greatly reduces the operational risk to a launch vehicle, or any hybrid rocket propelled missile or vehicle. Table 2.1 compares the characteristics of these three types of chemical rockets.

Table 2.1: Comparison of chemical rocket motor characteristics.

| Factor                                 | Solid      | Hybrid     | Liquid Bi-Propellant |
|--|------------|------------|----------------------|
| Command Shutdown & Throttle Capability | No         | <b>Yes</b> | <b>Yes</b>           |
| Non-Toxic Combustion Exhaust           | No         | <b>Yes</b> | Can be               |
| Ease of Transport, Storage, & Handling | No         | <b>Yes</b> | <b>Yes</b>           |
| Maintenance & Launch Processing Cost   | Moderate   | <b>Low</b> | Moderate to High     |
| Manufacturing Cost                     | Moderate   | <b>Low</b> | Moderate to High     |
| Readily Scalable                       | <b>Yes</b> | <b>Yes</b> | No                   |
| $I_{sp}$                               | Good       | Good       | <b>Excellent</b>     |
| Propellant Mass Fraction               | Good       | Fair       | <b>Excellent</b>     |
| Safe, Non-Explosive Propellants        | No         | <b>Yes</b> | Can be Minimized     |

## 2.1 Advantages of Hybrid Rocket Systems

Hybrid motors that employ non-toxic, non-explosive propellants have the potential to fulfill this market niche. Because the propellant components remain inert until ignited within the motor chamber, hybrid rockets are inherently safer to transport, load, store and operate [6]. This inherent safety greatly reduces ground handling and transportation costs, and can potentially lead to an overall reduction in system operating costs. Unlike solid-propelled rockets, where fuel grain flaws and age-induced cracks present a significant safety issue, hybrid rockets exhibit a relative insusceptibility to grain flaws. Other advantages of hybrid rockets that can potentially offset the lower performance level include the ability to be restarted in flight and the ability to be throttled over a significantly wider range of thrust levels compared to conventional liquid bi-propellant systems [7].

## 2.2 Technical Limitations of Hybrid Rocket Systems

Considering the above listed advantages, hybrid motors are not without technical difficulties and operational shortcomings. As mentioned hybrid rocket motors have traditionally suffered from two primary insufficiencies; 1) lower  $I_{sp}$  than conventional bi propellant liquid



and lower volumetric efficiency than of solid rockets of the same thrust level, and 2) low fuel regression rates. These low regression rates result in low fuel mass flow rates for a given oxidizer flux level. To achieve oxidizer-to-fuel (O/F) ratios that produce acceptable combustion characteristics traditional cylindrical fuel ports have been fabricated to have a very long length-to-diameter ratio. This high aspect ratio results in poor volumetric fuel loading and substantial unused residual fuel.

Of primary concern is the low fuel regression rate typically seen in hybrid rocket motors. A popular fuel for hybrids is HTPB, which is a legacy thermosetting polymer material that is mixed from its liquid base-components, degassed under vacuum, and then cast and cured in a fuel grain mold. HTPB does not melt in the presence of heat, but instead chars and ablates. The well-known blowing effect induced by the radial flow of this ablated fuel material generally results in low overall fuel regression rates [8]. Hybrid motors which are based on ablating fuel grains typically produce regression rates that are significantly lower than solid fuel motors in the same thrust and impulse class. Increasing the oxidizer mass flux increases fuel regression rates; unfortunately, the resulting combustion instabilities at high flux rates limit the effectiveness of this option [9].

### 2.3 Hybrid Design and Fabrication Methods

Unlike solid propellant motors, the fuel regression rate on hybrid rocket motors is significantly influenced by the oxidizer mass flux and the ratio of the fuel port surface burn area to the fuel port chamber volume. Fuel regression rates can be as much as 25-30% lower than solid fuel motors in the same thrust and impulse class. Thus to achieve oxidizer-to-fuel ( $\text{O/F } [\dot{m}_{ox}/\dot{m}_{fuel}]$ ) ratios that produce acceptable combustion characteristics traditional cylindrical fuel ports have been fabricated to have a very long length-to-diameter ratio. This high aspect ratio results in poor volumetric efficiency and substantial amounts of unused residual fuel.

The current fabrication method of standard HTPB fuel grains casts each grain by hand in a hand-molded combustion chamber casing to be later joined with other motor components (i.e., igniter, oxidizer tank, oxidizer valve/injectors, post combustion chamber,

and rocket nozzle) using a labor-intensive manual process. This low technology approach produces motors with a high degree of variability at unacceptable production costs. Thrust and impulse levels can vary by as much as 20%. This one-off production process cannot mass-fabricate hybrid fuel grains and motors at a rate that is anywhere near the rates required for commercial spaceflight operations, micro-satellite launches, or for air/ground launched missiles.

This high degree of motor-to-motor variability is acceptable for experimental vehicles, but will not allow FAA certification for non-experimental, commercial spaceflight operations. Additionally, motor-to-motor thrust variability produces significant thrust asymmetries for clustered hybrid motor configurations. This asymmetry represents a significant hazard and currently precludes using multiple hybrid motors clusters for launch vehicles. Because hybrid motor combustion physics require a longer aspect ratio when compared to their liquid and solid counterparts, structural aspects of this high aspect ratio prevent building a single hybrid motors that can produce sufficient thrust and impulse to achieve orbital velocity. Clustered motors will be required for hybrid motors to achieve low earth orbit. Finally, the current low-tech, labor intensive fabrication processes simply cannot produce the number of motors required to support launch rates necessary to allow the rapidly-growing commercial space ventures to be economically viable.

With FDM manufacturing, fuel grains that vary along the length of the grain also become possible. A fuel grain with a helical instead of a straight port has a significantly longer effective motor length, allowing for higher volumetric efficiency. With the improved manufacturing techniques and helix fuel grain, all of the weaknesses of a hybrid rocket motor are overcome. The embedded helical port provides a large surface contact area in a significantly shorter length than can be achieved with traditional cylindrical fuel port shapes. The centrifugal forces created by the combustion gases rotating in the helix core significantly increase the fuel regression rates and propellant mass flow. This design feature produces sufficient total fuel mass flow so that the total oxidizer to fuel ratio remains near optimal during the entire motor burn. Helical ports can be more than 50% shorter than

traditional cylindrical fuel ports and still produce the same thrust level.

FDM methods offer the potential to revolutionize hybrid fuel grain and rocket motor manufacturing. Leveraging FDM manufacturing means overhead of manufacturing a rocket no longer has to be carried by the aerospace industry alone. FDM manufacturing technology can support high production rates with a much greater degree of motor-to-motor consistency than is possible using traditional motor manufacturing methods. If matured and commercialized, this technology will have a transformational effect on hybrid rocket motor production by improving quality, consistency, and performance, while reducing development and production costs.

## Chapter 3

### Literature Survey

The earliest hybrid rocket motors, originally called 'solid-liquid' rockets, were developed (in parallel) in the late 1930's by B. Smith and R. Gordon who formed the California Rocket Society, as well as Oberth in Germany. These first hybrids used very unconventional fuels, such as graphite, which did not perform well due to an extremely low rate of ablation. In the 40's, the Pacific Rocket Society developed their Douglas fir rockets, or eXperimental Douglas Fir (XDF) rockets. After 23 design iterations, XDF-23 successfully launched in June of 1951 using a liquid oxygen (LOX)-rubber motor [10]. Since then, hybrid motor development has taken off, with many more static tests and successful rocket launches. The typical modern hybrid motor consists of a Hydroxyl-Terminated PolyButadiene (HTPB) fuel grain with a cylindrical oxidizer port, and a liquid or gaseous oxidizer, such as: liquid  $O_2$ , gaseous  $O_2$ , or  $N_2O$ . Additives such as aluminum powder are often used to increase the performance of the hybrid motor by increasing fuel density, flame temperature, and regression rate.

Since the inception of hybrid rockets, a great deal of research has been done on hybrid fuel/oxidizer additives and alternatives, often resulting in regression rate and specific impulse (Isp) increases over standard HTPB and  $N_2O$ . Fuels such as paraffin [11], ethanol-based gels [12], polymethyl methacrylate (PMMA), high density polyethylene (HDPE), sorbitol [13], and even lard [14] have been researched. Most of these alternative fuels have increased regression rates, but are much more complex to cast/machine, or are simply fragile. Oxidizers such as hydrogen peroxide [15,16], oxygen doped with fluorine (FLOX) [17], and red fuming nitric acid (RFNA) [10] have been investigated. Both hydrogen peroxide and FLOX have Isp's higher than  $N_2O$ , but are more difficult to handle. In the case of FLOX, it is one of the highest performing oxidizers known, with an Isp in the 400's, but is

also one of the most toxic! Fuel additives including varying sizes and grades of aluminum powders [17–20], ammonium perchlorate [21], iron oxide, copper chromite [22], triethylaluminum, diisobutylaluminum hydride, and lithium aluminum hydride  $LiAlH_4$  [23] have also been investigated, all of which do enhance regression rates to some degree. Combinations of exotic fuels/oxidizers/additives have also been investigated [20, 23–25], with regression enhancements varying from none to a factor of 7 (by mass). All of this research clearly illustrates the flexibility of hybrid rockets, as there are even more options for hybrid fuels, oxidizers, and additives not mentioned that would still be effective.

Current hybrid research at Utah State University typically uses  $N_2O$ /HTPB motors because of the non-toxicity and ease of handling. Lockheed Martin and the Environmental Aerospace Corporation [26] has done work characterizing  $N_2O$ /HTPB motors much like the ones used at Utah State. Stanford [27, 28] has done an extensive amount of work on large-scale liquid oxygen (LOX) and paraffin rockets, including several successful static test firings.

Research performed at Utah State University [1] and The Aerospace Corporation [5] has investigated using ABS plastic as an alternative fuel, which can be either extruded or rapid prototyped into any shape desired. This fuel is mechanically robust, with performance only slightly lower than the industry-standard fuel, HTPB. Using Fused Deposition Modeling (FDM) techniques, a helix fuel grain can easily be printed in ABS plastic, rather than attempting to cast a fuel grain out of HTPB with a helical mandrill. This approach allows for geometrically complex fuel grains to be produced quickly and easily.

Solid rocket motors have been designed with non-circular oxidizer ports for many years. Typically, these non-circular patterns consisted of stars or “wagon-wheel” designs. These patterns were created to match a specific thrust profile during flight [29]. Because of significantly different combustion physics, the purpose of complex geometry in hybrids is different. Instead of thrust profiles, the intent of complex geometry is to simply increase the burning surface area of the fuel grain, such that fuel vaporizes at a rate sufficient to produce thrust as high as solid rocket motors with an acceptable O/F ratio to maintain efficient

combustion.

In the 60's, under Air Force Sponsorship, the United Technology Center conducted the first large-scale wagon-wheel test fires. Figure 3.1 shows a photograph of the pre- and post-burn fuel grain [10].

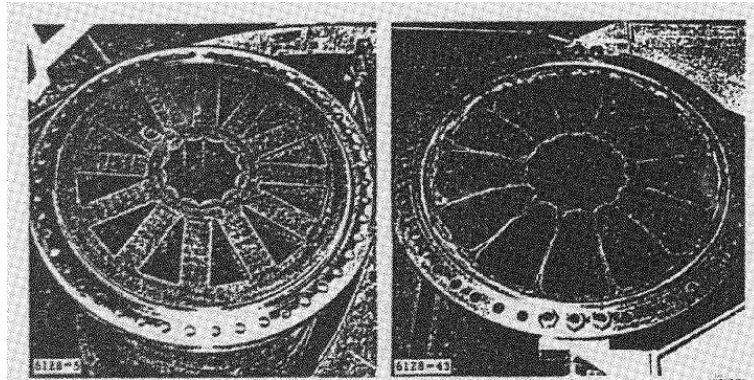


Fig. 3.1: Hybrid wagon-wheel fuel grain.

Figure 3.1 shows a 38" (96.5 cm) diameter motor, 40,000 lbf (180 kN) thrust, which demonstrated comparable thrust levels to solid motors of the time. These complex geometries, however, tend to shift the oxidizer to fuel ratio away from the optimal, and often will leave behind unburned fuel slivers. These slivers are clearly visible in Figure 3.1 and, reduce the mass efficiency. The Sierra Nevada Corporation [30] uses a wagon-wheel design for their Dreamchaser and SpaceShip Two motors to obtain the thrust levels required for their launch vehicles.

Some of the earliest hybrid motors regression rate research was performed by Marxman [8] in the 1960's, who derived one of the first regression rate equations for a hybrid motor based on physical models. During the same time period, Rocketdyne [31] also conducted extensive research in hybrid motor regression, experimenting with different additives to the fuel, and obtained longitudinal measurements of regression as a function of axial distance. More recently, Utah State University [32] investigated hybrid regression using a one-dimensional surface turbulence model, which was also verified through testing.

## Chapter 4

### Regression Modeling

Two fundamentally different processes drive solid and hybrid fuel grain regression rates. This section will present an overview of each, and discuss both past and state of the art in regression rate modeling for both solid and hybrid rockets. The burn back rate of the fuel port is often modeled by a linear regression, where for a given fuel port cross section the fuel burns at a prescribed rate normal to the local surface. Typically this propellant regression rate is modeled as a 2-dimensional longitudinal average where the port burns back at the same rate along the length of the motor fuel port. Figure 4.1 illustrates this concept.

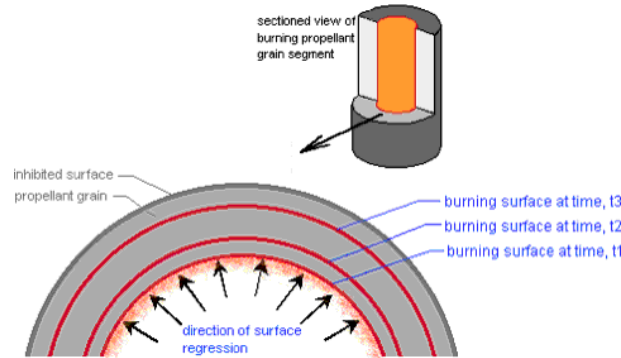


Fig. 4.1: Linear fuel port regression.

#### 4.1 Solid Propellant Fuel Grain Regression Modeling

Solid propellants are blended using a combination of oxidizer and fuel in a mass proportion that delivers the optimized performance for a given mission requirement. Because the propellant mixture ratio is set by the original formulation, the O/F remains constant throughout the burn, and the surface regression rate can be described by the well-known Saint-Roberts law:

$$\dot{r} = aP_0^n. \quad (4.1)$$

In Eq. (4.1)  $\dot{r}$  is the fuel regression rate normal to the fuel surface,  $P_0$  is the chamber pressure of the rocket, and the parameters  $\{a, n\}$  are empirical constants that are a function of the propellant formulation, density, level of metallization, and oxidizer grain size. The propellant mass flow is generated by combustion is:

$$\dot{m}_{propellant} = A_{burn}\rho_{propellant}\dot{r} \quad (4.2)$$

In Eq. (4.2)  $A_{burn}$  is the burning surface area, and  $\rho_{propellant}$  is the propellant density. Table (4.1) shows the burn rate parameters for various solid propellant formulations.

Table 4.1: Saint Robert's curve fits for various solid propellants.

| Propellant Name                      | n        | a ( $in/s \cdot psia^n$ ) |
|--------------------------------------|----------|---------------------------|
| Composite Ammonium Nitrate, -40F     | 0.463474 | 0.002965                  |
| Composite Ammonium Nitrate, 60F      | 0.445084 | 0.003909                  |
| Composite Ammonium Nitrate, 140F     | 0.426803 | 0.005243                  |
| High Energy XLDB Composite           | 0.720473 | 0.002293                  |
| Composite Ammonium Perchlorate, -30F | 0.187867 | 0.072001                  |
| Composite Ammonium Perchlorate, 60F  | 0.170286 | 0.094044                  |
| Composite Ammonium Perchlorate, 150F | 0.172255 | 0.107348                  |
| JPN-type Double Base, 10F            | 0.712606 | 0.003818                  |
| JPN-type Double Base, 70F            | 0.701667 | 0.004624                  |
| JPN-type Double Base, 130F           | 0.678433 | 0.006260                  |
| High Burn Rate Composite @ 68F       | 0.380710 | 0.126409                  |

When coupled with the nozzle geometry and combustion properties for the specific propellant formulation, the operating chamber pressure directly influences the delivered motor thrust and impulse profile. Key factors in burn profile shaping for solid motors include the propellant burn exponent (n), and exposed surface area-to-port volume as the fuel grain burns and opens up. Figure (4.2) shows several geometries used to produce



various solid motor burn profiles.

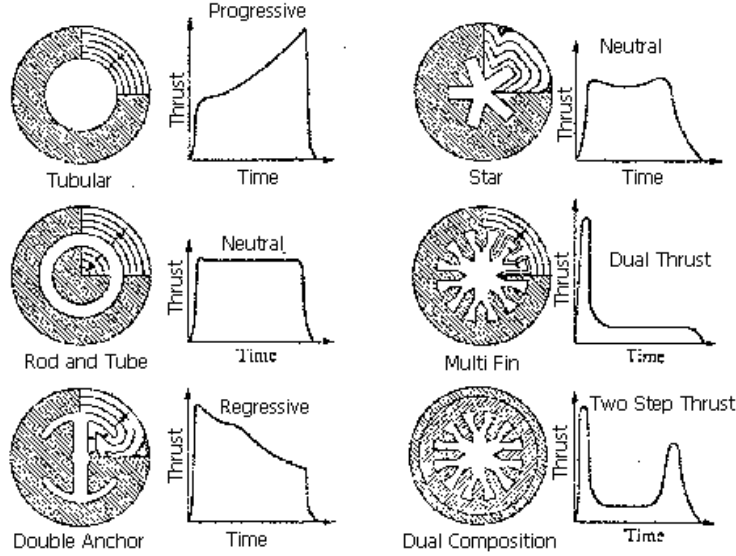


Fig. 4.2: Solid propellant grain port geometries and corresponding burn thrust profiles.

## 4.2 Two-Dimensional Hybrid Fuel Grain Modeling

Unfortunately, tailoring the hybrid grain geometry to achieve a prescribed thrust profile is significantly more difficult than with solid propellants where the combustion chemistry can be precisely controlled by a-priori formulations. Although the ratio of the propellant grain surface area to chamber volume has an influence on the evolving chamber pressure as with a solid motor, the oxidizer feed mass-flow also has a very significant effect and the burn profile is a function of a whole suite of control variables. A motor with a particular fuel grain pattern that behaves in one manner for a given propellant combination and initial mixture ratios will perform significantly differently for a different combination of propellants.

In contrast to solid rocket motors, the combustion process for hybrid motors is significantly more complex. With hybrid rocket motors as the fuel grain burns and the surface geometry changes, the oxidizer mass-flux also changes. This changing mass flux in turn changes the solid fuel regression rate and alters the thermodynamic and transport properties of the combustion products. The O/F ratio varies continuously throughout the motor burn. The primary consequence of the hybrid flow physics is that regression rate-models

based on St. Roberts law are inaccurate. Several studies have demonstrated that hybrid fuel regression rates have little or no dependence on chamber pressure [29].

Marxman and Gilbert first proposed an enthalpy-based fuel regression model for hybrid rocket motors in the early 1960s [33]. The fundamental assumption made by Marxman and his colleagues was that regression rates in a hybrid rocket are dominated by thermal diffusion and not chemical kinetics [8]. Consequently the fuel surface regression is strongly a function of turbulent boundary-layer heat transfer. Boundary layer mixing creates a region where oxidizer flow from the center of the motor combustion port mixes with vaporizing solid fuel leaving the fuel wall. Close to the fuel wall is the flame zone where the combustion of fuel and oxidizer primarily takes place. Heat transfer from this zone to the solid fuel grain drives the regression rate behavior of hybrid rocket motors.

Later studies performed by Strand [34] and later Chiaverini et al. [35] showed that the experimental coefficients predicted by Marxman, specifically the exponents on mass flux and the surface blowing coefficient, were substantially different from the theoretical values derived in the classical relation. Due these deviations from the experimental data, the original form of the model derived by Marxman model is not often used in modern hybrid rocket performance analyses. Additionally, the Marxman model relates the fuel regression rate to the surface skin friction, but does not close sufficiently to allow a priori regression rate predictions [36].

A closed-form regression rate model based on flat-plate flow theory was developed by Eilers and Whitmore [32] and corrected by Whitmore and Chandler [37] for non-unity Prandtl number

$$\dot{r} = \frac{0.047}{Pr^{0.153} \rho_{fuel}} \left( \frac{c_p [T_0 - T_{fuel}]}{h_{v_{fuel}}} \right)^{0.23} \left[ \frac{\dot{m}_{ox}}{A_{chamber}} \right]^{\frac{4}{5}} \left( \frac{\mu}{L} \right)^{\frac{1}{5}} \quad (4.3)$$

In Eq. 4.3 the parameters  $\mu$  and  $Pr$  refer to the combustion product gas properties, and  $c_p$ ,  $\rho_{fuel}$ ,  $T_{fuel}$ , and  $h_v$  refer to the properties of the solid fuel grain. Equation 4.3 predicts rate of regression for the entire motor averaged longitudinally along the length of the motor.

The model of Eq. (4.3) was developed from an enthalpy balance between the latent heat of the burning fuel and the heat convection into the combustion flame zone. Applying the generalized (non-unity Prandtl number) form of the Reynolds analogy between the Stanton number and the surface skin friction coefficient allows the heat transfer coefficient to be calculated. The model uses the Reynolds-Colburn analogy to relate the heat transfer at the surface of the fuel grain to the local boundary layer heat transfer, and overcomes the shortcoming of Marxman's original model.

In Eq. (4.3) the oxidizer mass flow rate of  $N_2O$  is modeled by the incompressible discharge coefficient formula

$$\dot{m}_{ox} = A_{ox} C_{d_{ox}} \sqrt{2\rho_{ox}(P_{ox} - P_0)} \quad (4.4)$$

The parameters  $P_{ox}$  and  $\rho_{ox}$  refer to the incompressible oxidizer liquid properties upstream of the injector, and  $A_{ox}$ ,  $C_{d_{ox}}$ ,  $A_{chamber}$ , and  $L$  are the injector discharge area, fuel port cross sectional area, and fuel grain length, respectively. Equation (4.4) is reasonably accurate as long as the motor is burned using a top pressure that is higher than the saturation pressure of the  $N_2O$  at the injector temperature. For blow down systems that use only the natural vapor pressure of the oxidizer, a more complicated two-phase model is required to accurately model the injector mass flow [37]. For purely compressible gaseous oxidizer flows, the oxidizer mass flow rate becomes

$$\dot{m}_{ox} = C_d A_{ox} \sqrt{\frac{2\gamma}{\gamma-1} \rho_{ox} P_{ox} \left[ \left( \frac{P_0}{P_{ox}} \right)^{\frac{2}{\gamma}} - \left( \frac{P_0}{P_{ox}} \right)^{\frac{\gamma+1}{\gamma}} \right]} \quad (4.5)$$

Observing both equations (4.3) and (4.4), it can be noted that the third term in Eq. (4.3) is actually the mean oxidizer mass flux through the port, where oxidizer mass flux is defined as

$$G = \frac{\dot{m}_{ox}}{A_{chamber}} \quad (4.6)$$

This comparison supports Marxman's original assertion that oxidizer mass flux is a

major driving factor in hybrid fuel grain regression rates. The total fuel mass flow rate can be calculated from the regression rate model by

$$\dot{m}_{fuel} = A_{burn}\rho_{fuel}\dot{r} \quad (4.7)$$

In Eq. 4.7,  $A_{burn}$  is the total fuel port surface area. The oxidizer to fuel ratio (O/F ratio) is therefore given by

$$O/F = \frac{\dot{m}_{ox}}{\dot{m}_{fuel}} = \frac{A_{ox}C_{d_{ox}}\sqrt{2\rho_{ox}(P_{ox} - P_0)}}{A_{burn}\rho_{fuel}\dot{r}} \quad (4.8)$$

Clearly, examining Eq. (4.3) and (4.8) show that as the fuel grain burns and the surface burn area changes, O/F ratio will vary significantly. Since the O/F ratio is highly dependent on the mean oxidizer mass flux, the chamber pressure clearly will be a major driver in the overall mean regression rate.

Assuming the nozzle throat chokes immediately, a balance between the gases coming into the fuel port and the gases leaving through the choked throat determines the time response of this chamber pressure growth. Here the equation that describes the time evolution of the chamber pressure is

$$\frac{\delta P_o}{\delta t} = \frac{A_{burn}\dot{r}}{V_c} [\rho_{fuel}R_gT_o - P_0] - P_0 \left[ \frac{A^*}{V_c} \sqrt{\gamma R_gT_0 \left( \frac{2}{\gamma+1} \right)^{\frac{\gamma+1}{\gamma-1}}} \right] + \frac{R_gT_0}{V_c} \dot{m}_{ox} \quad (4.9)$$

In Eq. 4.9,  $T_0$  is the combustion flame temperature at the current O/F ratio and  $V_c$  is the total fuel port volume, including both pre- and post-combustion chambers. Equation 4.3 is derived based on the assumption that typical hybrid motors have very long aspect ratios with length to diameter ratios greater than 20. Along the entire length of the motor, fuel is being dumped into the core oxidizer flow. This process does not allow fully developed channel flow to develop until far down stream in the fuel port. For this analysis, a simple empirical skin friction model based on 2-dimensional boundary layer theory was used in lieu of a fully developed model for pipe-flow skin-friction. Figure 4.3 depicts the proposed

boundary layer growth process.

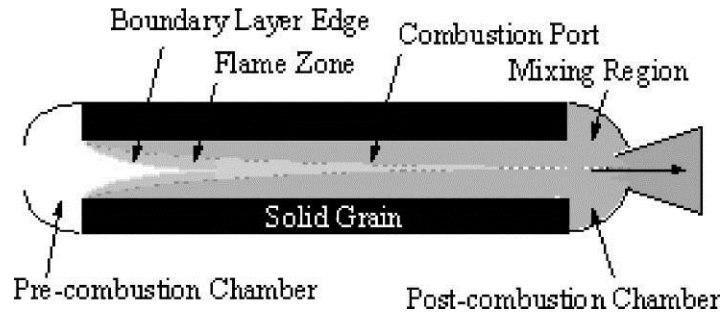


Fig. 4.3: Longitudinal boundary layer development within the fuel port.

Experimental tests performed by Whitmore and Peterson [1] with both HTPB ABS fuel grains support the accuracy of this undeveloped flow assumption. Figure 4.4 shows side-by-side comparisons of post 10-second burn HTPB and ABS fuel grains. The regression measurement stations are marked on each grain. For both the HTPB and ABS grains, fossilized surface flow patterns are visible, and the transition from laminar to turbulent flow patterns is clearly visible. The surface burn patterns transition from laminar to turbulent moving aft along the motor flow channel. The flow patterns are very similar to the classical flat plate flow transition pattern.

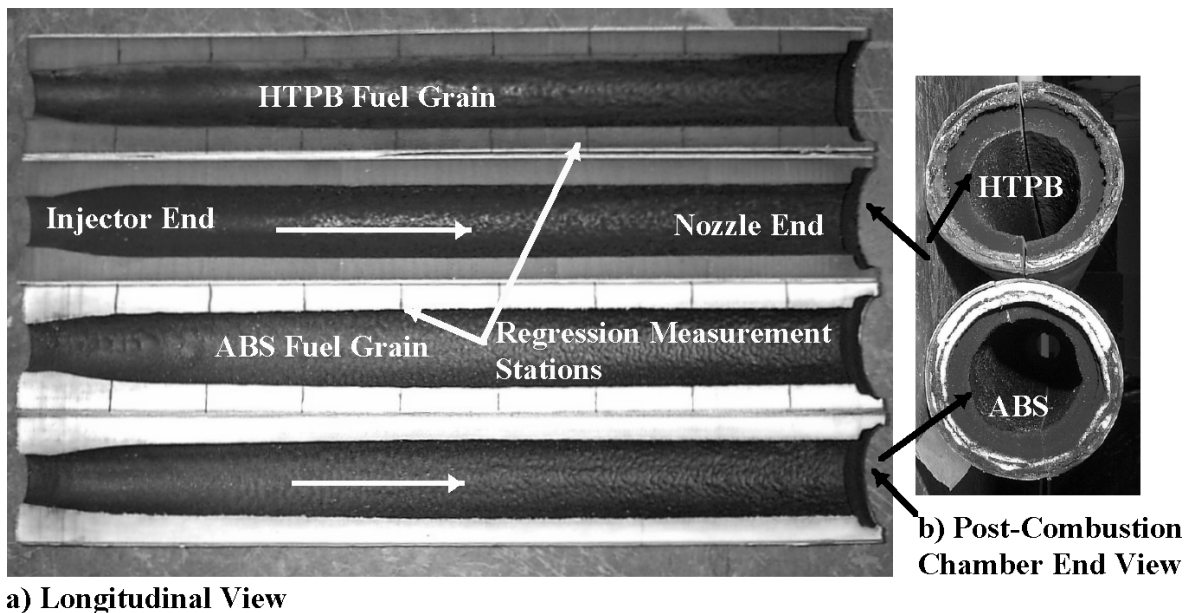


Fig. 4.4: Burned HTPB and ABS fuel grains.

Figure 4.5 plots the longitudinal-mean regression-rate measurements of the HTPB and ABS burns performed by Whitmore et al. [1] against the mean oxidizer mass flux for the burn. These data are compared with the analytical model predictions of Eq. 4.3. Following the end of each static test, the motor was quenched and then split longitudinally to expose the burned grain pattern. The final regression dimensions were measured at multiple points along the fuel grain, and the mean end-to-end longitudinal fuel regression was calculated. The mean regression rates were calculated using the two of the methods developed by Karabeyoglu et al. [38] based on the mean longitudinal change in diameter divided by one-half of the burn time and the overall change in propellant mass divided by the burn time.

The mean oxidizer mass flux is calculated using the mean of the initial and final port diameters. These comparisons verify the ability of Eq. (4.3) to accurately predict the mean longitudinal rate of regression for hybrid fuel grains, based on a priori knowledge.

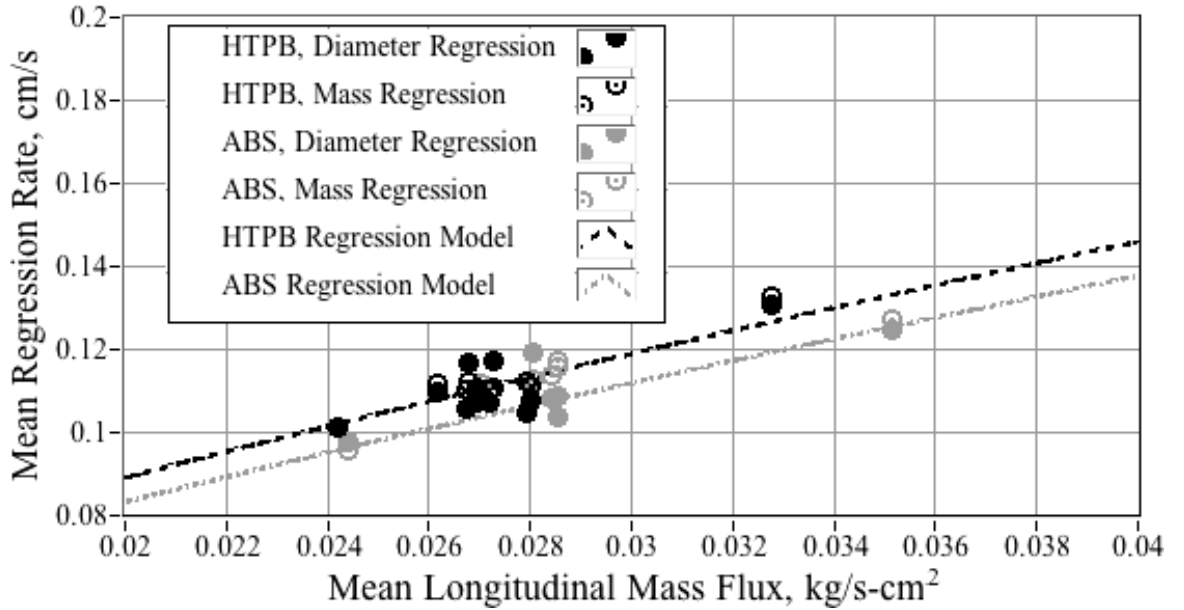


Fig. 4.5: Predicted and measured linear regression for HTPB and ABS grains. [1]

### 4.3 Three-Dimensional Hybrid Fuel Grain Regression Modeling

The hybrid fuel regression rate model developed in the previous section has two significant shortcomings: 1) generally an analytical representation of the fuel port is required in

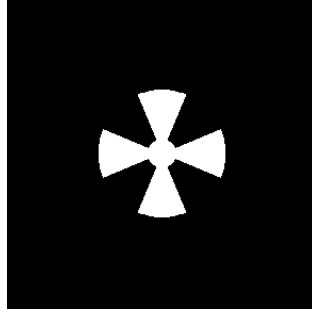
order to keep track of the changes in the fuel port surface area, cross sectional area, and port volume as the grain recedes. This limitation has typically restricted the applications of the model to very simple fuel grain geometries like cylindrical ports. A second limitation is the 2-dimensional nature of the model. The fuel grain regression predictions are longitudinally averaged along the length of the fuel port. The images presented Figure 4.4 clearly show that the linear regression within the fuel port occurs in 3-dimensions with the cross section regression changing as a function of the longitudinal location within the fuel port.

Accurately modeling helical fuel grain regression rates will clearly require a 3-dimensional calculation. Regression rates in a helix grain, however, will be quite different from those rates that occur in a circular fuel port. There have been no published papers on using a helical fuel port in a hybrid or solid fuel grain, but there have been several papers investigating friction and heat transfer in helical tubes in similar flow regimes. The original work on flow through curved tubes was done by Dean [39, 40], who developed a modified Reynolds number for helical flow - the Dean number. Mishra et al. [41] investigated momentum transfer in curved pipes, experimentally determining friction amplification factors over a wide range of pipe sizes and Reynolds numbers. Havas et al. [42] performed experiments on heat transfer in helical coils of agitated vessels, yielding a curve of heat transfer coefficient vs. Reynolds number. Another study by Yang et al. [43] investigated the heat transfer of a simple varying-curvature curved pipe, which yielded heat transfer coefficients and frictional coefficients over various Reynolds numbers.

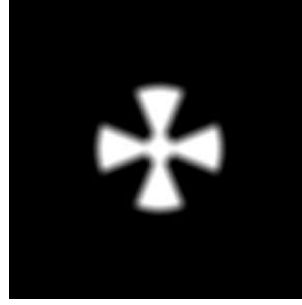
These studies all investigate fully developed flow, which is not the case for short helix fuel grains, but some order-of-magnitude friction and heat transfer estimates may be found from them. More significantly, these studies all assumed fixed surface boundaries, and provide no mechanism to numerically propagate the fuel grain surface boundary as the surface regresses. This paper will develop a novel method whereby the fuel cross section will be modeled as an array of gray-scale pixels and image-processing techniques will be used to regress the fuel grain geometry.

Figure 4.6 shows an example of this process. If a binary image of the grain is used

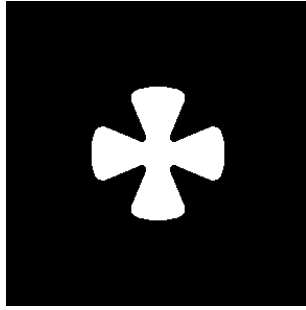
(Figure 4.6a), its edges can be blurred using an image filter (Figure 4.6b), and then all non-binary pixels in the image are removed (Figure 4.6c). The fuel is then regressed by the radius of the blur filter (Figure 4.6d).



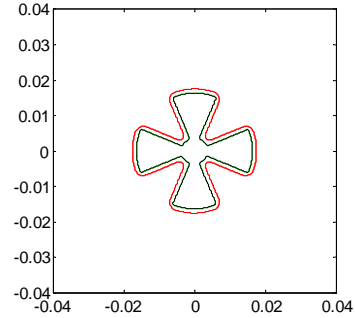
(a) Initial grain. (900x900 pixels)



(b) Blurred with a 40 pixel radius disk filter.



(c) Blurred Image with non-binary pixels removed.



(d) Borders regressed via blur filter.

Fig. 4.6: Geometric regression via blurring.

This technique produces comparable results to numerical propagation of the surface boundary. Additionally, blurring filters round sharp edges, which is difficult to do using geometric propagation. Sharp edges are rounded in hybrid motor grains during burns due to including boundary layer effects and heat transfer concentrations. This method also works for any grain geometry, not just simple geometric shapes. Figure 4.7 shows an example where the blurring technique is used to regress a complex, arbitrary shape.





Fig. 4.7: Arbitrary grain geometry regressed  $3 \frac{\text{pixel}}{\text{iteration}}$

The geometric propagation of fuel/propellant grains is a subset of accurate regression rate modeling. There has not been a great deal of development in this field, since previous regression rate prediction models have relied on parametric surface models to represent the fuel grain surface [44]. There are several different possibilities for geometric propagation that have been investigated [2]. The early computer models for grain geometry propagation involved intersection 3-D surfaces of blocks, cylinders, cones, spheres, and toroids [45, 46]. This method is effective at accurately modeling a grain, but it can be difficult to create an accurate initial grain model with the shapes available. Sethian [47] has developed a numerical method for propagating a 2-D surface via the Hamilton-Jacobi equations and conservation laws. This algorithm creates a 3D surface and then moves a 2D plane down the surface, the distance along the 3D surface proportional to burn depth, such as shown in Figure 4.8.

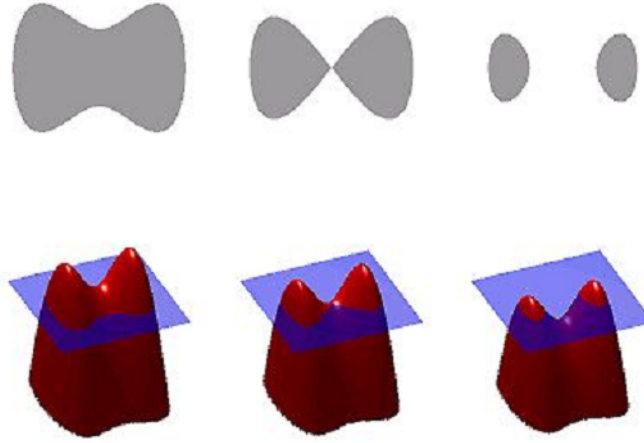


Fig. 4.8: Fast marching algorithm example [2]

This method is a popular one [48–50], as it is able to process most geometries with relative accuracy, including the handling of cusps and islands. This algorithm, however, is quite slow. It is also not possible to look at an arbitrary time stamp without calculating all previous times. Another approach is to propagate a 3D surface using a minimum distance function [51]. This method takes a 3D surface of triangles generated from a CAD file, and propagate them normal to themselves. This method is particularly useful for shapes that vary in the  $z$ -axis. It is also convenient in that the grain can be generated in any generic CAD program and imported, and any results can be similarly exported in the same format. Like the fast-marching algorithm, this method is also very slow, especially if the number of triangles (i.e. grid size) becomes large. This method also loses accuracy when converting smooth surfaces into triangles.

Hejl and Heister [52] developed a method to propagate surfaces by creating points along an axisymmetric surface, redistributing these points to concentrate on regions with curvature, as straight sections can be described accurately with only the endpoints. These grid points were then regressed normal to the grid points, and then the grid redistributes points again. This method works well with axisymmetric grains, and unique grains can be quickly generated with this method, but very sharp points in the grains remain as sharp

points unless they are regressed by some other section. This method is relatively popular, and has been used by many others [2, 44–51, 53–55].

Another method that has been investigated is to utilize the surface offset function available in many CAD programs to regress the grain [53–55]. A grain is parametrically generated in Matlab, exported to a CAD program and regressed, and then imported back into Matlab for surface area and volume calculations, and iterated through a burn. This method is fairly easy to implement, as it uses already-available software routines to regress a 3D surface, but these routines do not accurately recreate regression that would occur during a burn, and they are also very slow.

The closest approach to the image processing method chosen is described by Arnon [2] is the cellular automation method. It also turns a grain into a grid of cells or pixels, which each cell containing information about its state. Generally, these information states are “burning,” “propellant,” and “no propellant.” The algorithm then scans each cell and updates its state according to a set of rules. If the cell state is burning and the adjacent cell is not burning, then the adjacent cell is set to burning. If cell state is burning, then change to no propellant. The distance at which a cell is considered adjacent is the biggest sensitivity factor in the calculation. This method is very nearly what the image processing method does, except that instead of looping through each pixel and running a set of if statements, a disk blurring filter is applied to the image. Without this image processing technique, this method is slow and impractical. When the image filter is used, each iteration takes a fraction of a second, making for a relatively fast algorithm.

## Chapter 5

### Research Objectives

- Create a 2-D hybrid burn model using the image blurring regression
- Compare model results to previous burn data
  - Extract total regression and regression rate data from previously burned fuel grains with circular ports (see Table 5.1)
  - Extract total regression and regression rate data from previously burned fuel grains with complex port geometry (see Table 5.1)
    - \* One 2-D Maltese cross grain
    - \* Two helical grains
- Improve model if inconsistencies are found between model and test data
  - Edge rounding
  - Regression rates
- Model regression profile of (2) new grain geometries - Maltese Cross and “Goldfish” (see Table 5.2)
  - Burn each fuel grain up to (4) times for 2 seconds each, taking regression measurements at each burn
- Compare results of model and prediction
- Complete 2 additional burns of a motor with helical fuel port (see Table 5.2)
  - Characterize effects of fuel port pitch angle on regression rate

– Estimate internal helix port flow characteristics

\* Reynolds Number

\* Friction Coefficient

Table 5.1: Previous burn geometries to be analyzed.

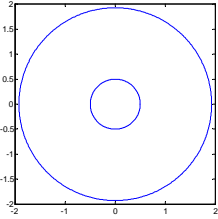
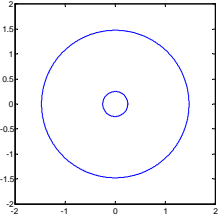
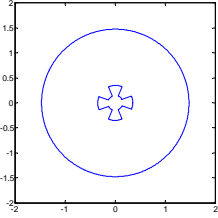
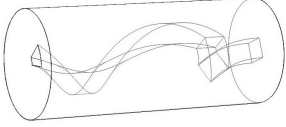
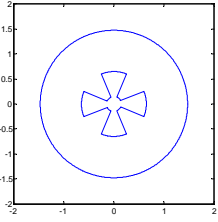
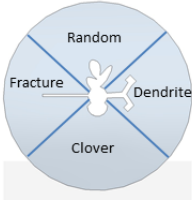
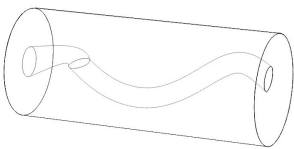
| Grain Type            | Grain Image   | Length | Port Diameter   |
|-----------------------|---|--------|-----------------|
| 3.86" (98mm) Circular |   | 12"    | 1"              |
| 2.95" (75mm) Circular |  | 12"    | 0.5"            |
| Maltese Cross         |  | 12"    | ID=0.3" OD=0.7" |
| Helix - Low Pitch     |  | 6"     | 0.5"            |

Table 5.2: New burn geometries to be analyzed.

| Grain Type         | Grain Image  | Length | Port Diameter     |
|--------------------|--|--------|-------------------|
| Maltese Cross      |   | 6"     | ID=0.3" OD=1.3"   |
| "Goldfish"         |   | 6"     | 4-sectional grain |
| Helix - High Pitch |  | 6"     | 0.5"              |

## Chapter 6

### Geometric Regression Model Development

#### 6.1 Geometric Regression Algorithm

The geometric regression uses a 2D, binary image of a fuel port for the initial, unburnt grain. The edges of the picture are assumed to be the case radius. The picture is stored as a matrix  $\bar{I}$ , where the index of the matrix corresponds to the (x,y) position, and value in each matrix cell is a gray-scale value (between 0 and 1). The example in Figure 4.6 is 900x900 pixels. The conversion factor between pixels and any arbitrary unit is then simply:

$$dx = \frac{W}{n_{px}}, \quad dy = \frac{H}{n_{py}} \quad (6.1)$$

where  $W$  is the width of the image in meters,  $H$  is the height of the image in meters, and  $n_{px}$  and  $n_{py}$  are the number of pixels in the x and y dimensions of the picture.

Before the image is regressed, important geometric properties of the grain can be easily extracted. Using the “bwboundaries” function in Matlab, the  $\bar{X}$  and  $\bar{Y}$  vectors of the boundary between the black and white edges of the picture are returned. The perimeter of the port is then:

$$P = \sum \sqrt{(\delta\bar{X} \cdot dx)^2 + (\delta\bar{Y} \cdot dy)^2} \quad (6.2)$$

where  $\delta\bar{X}$  and  $\delta\bar{Y}$  are the difference vectors of  $\bar{X}$  and  $\bar{Y}$  respectively, such that

$$\delta\bar{X} = \begin{bmatrix} \bar{X}(2) - \bar{X}(1) & \bar{X}(3) - \bar{X}(2) & \dots\dots & \bar{X}(n) - \bar{X}(n-1) \end{bmatrix} \quad (6.3)$$

The port area calculation is even simpler

$$A_{port} = \sum_{i=1}^n \left[ \sum_{k=i}^m [\bar{I}(i, k)] \right] \cdot dx \cdot dy \quad (6.4)$$

where  $n$  and  $m$  are the dimensions of  $\bar{I}$ .

Using the equations from the previous section, oxidizer mass flux  $G$  and  $\dot{r}$  can be calculated. With these values known, the image can now be regressed. To regress the image, a disk filter of radius  $\dot{r}dt$  (converted to pixels) is applied to the image. This disk filter moves through each pixel in the image and takes a spacial average of all of the pixels within the radius of the filter. This average is then the new value of the pixel. In Matlab, this is done using the `imfilter` function, which converts the image to the frequency domain and performs a low pass filter on the image, and then converts the image back to the 1-D domain.

The image is then thresholded such that any pixels that are not perfectly black (zero) are regressed and turned white (one). Thresholding creates a new binary image of the fuel grain that has regressed by  $\dot{r}dt$  pixels. The port perimeter and area are calculated again, which yields a new  $\dot{r}$ , and a new disk filter of size  $\dot{r}dt$  is created. This process is then looped through the desired burn time. Figure 6.1 shows a fuel grain regressed at a constant regression rate using this algorithm at an arbitrary regression rate of 15 pixels/iteration until it reaches the case.

Note that this does not round edges as much as what might be expected in a true burn. This is because there is no weight factor that causes protruding corners to regress faster, and recessed corners to regress slower. To remedy this, a non-zero threshold level can be used. In order to increase how much sharp corners are rounded, the threshold used can be changed to some value between 0 and 0.5. This means that instead of making all pixels that are gray completely white, make only a chosen percentage of them white, and the rest black. This is a much more accurate method of regressing a fuel grain. With a non-zero threshold, fractures no longer immediately regress, as the disk filter only slightly grays the region, and is then turned back to black. This phenomenon is analogous to heat transfer to the fuel grain. The reason that sharp edges become blunt during a burn is because of



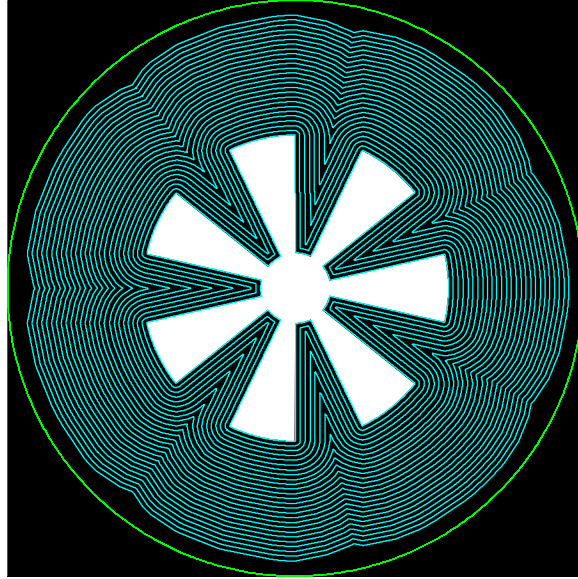


Fig. 6.1: Example fuel grain regressed with zero threshold

a concentration of heat transfer to a relatively small surface, which then erodes the sharp edge faster than other geometric sections that do not concentrate heat transfer.

With this non-zero threshold, the grain will no longer regress at exactly the radius of the disk filter. This means that the disk filter radius is no longer  $\dot{r}$ , but is instead  $\dot{r}dt - M$ , where  $M$  is the number of pixels removed by the threshold. In order to determine  $M$ , the 'shape' of the resulting disk filter must be characterized. Figure 6.2 shows a zoom up of a simple line with a disk filter applied. This particular disk filter had a radius of 8 pixels. This means that the distance (in pixels) from the perfectly black section to the perfectly white section is 16 pixels.

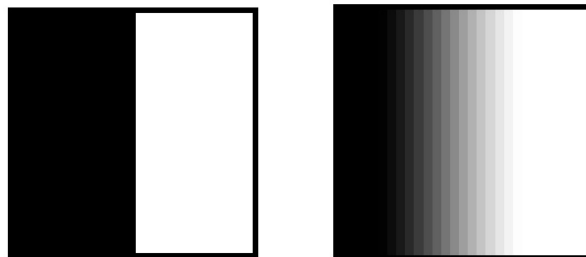


Fig. 6.2: Basic disk filter example

This variation between black and white is not perfectly linear. It follows a 3rd order polynomial, as shown in Figure 6.3. This particular curve is for a disk filter of radius 15.

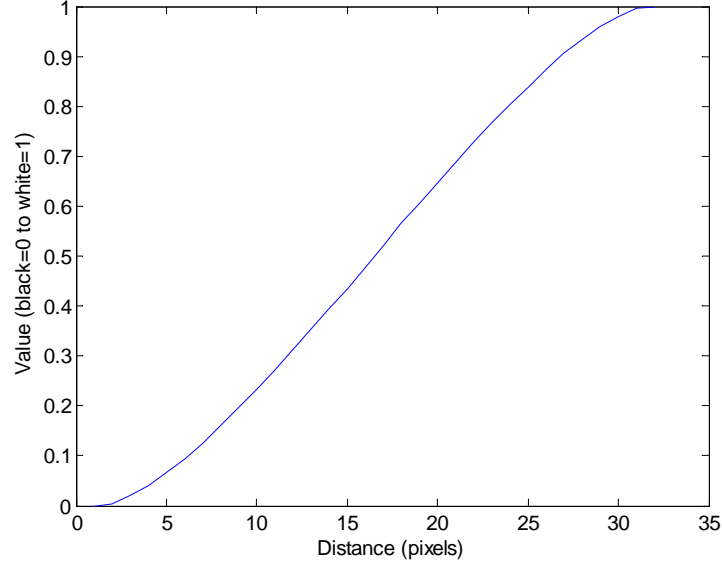


Fig. 6.3: Disk filter fit curve

The desired regression rate,  $\dot{r}_{desired}$  is then input into a function that calculates the value of  $\dot{r}dt - M$ , and iterates the input value of  $\dot{r}$  until the value of  $\dot{r}dt - M = \dot{r}_{desired}$ . Figure 6.4 illustrates the effect of changing the threshold amount with this compensation.

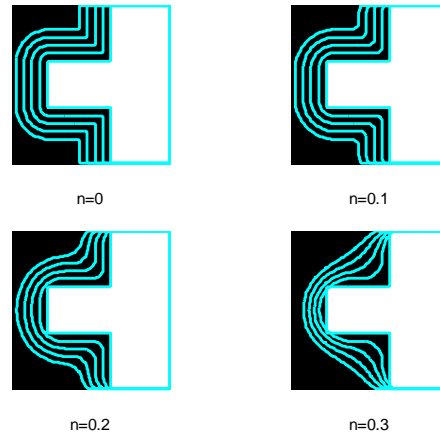


Fig. 6.4: Thresholding examples

Figure 6.5 shows the exact same grain as shown in Figure 6.1, regressed with a disk filter of size  $\dot{r}dt + M$ , and a threshold of 0.35.

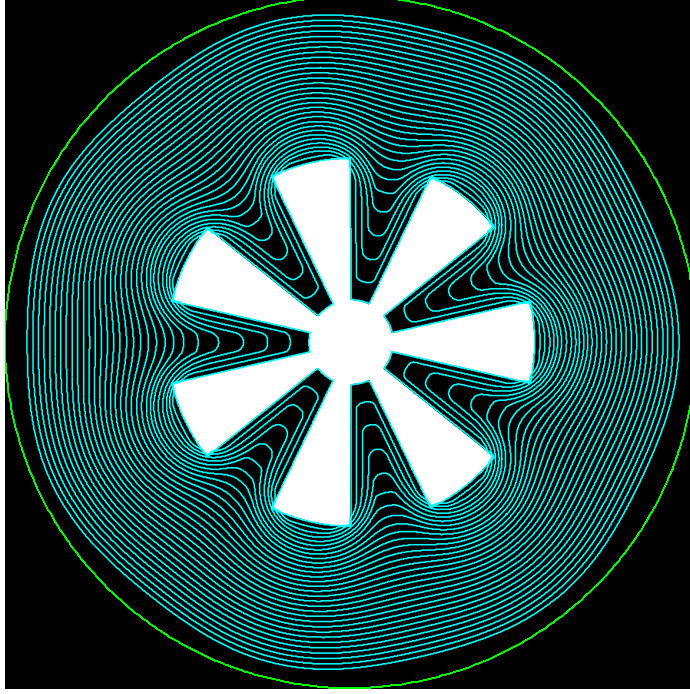


Fig. 6.5: Example fuel grain regressed with a 35% threshold

With a proper threshold amount selected, the fuel will regress in a manner that is more consistent with an actual burn. The geometric propagator is now robust enough to use in a full burn simulation, integrating  $\dot{P}_0$ , and  $\dot{r}$  to predict motor performance. Figure 6.6 shows a block diagram of the total algorithm:

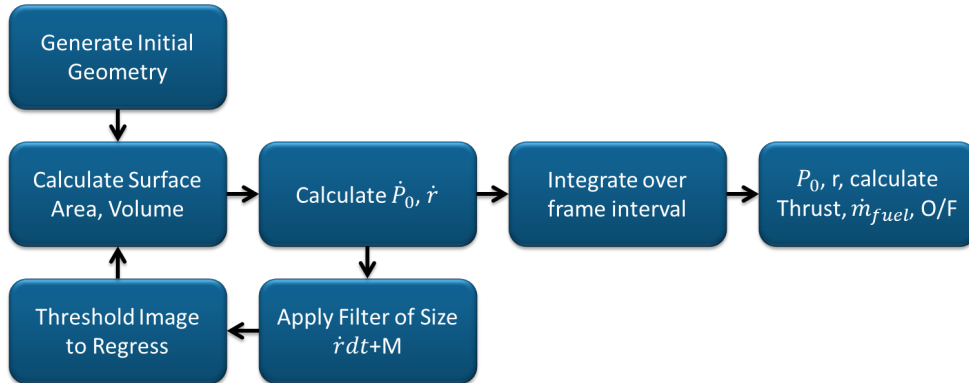


Fig. 6.6: Software algorithm block diagram.

## Chapter 7

### Results

#### 7.1 Motor Testing

Motor static ground testing was performed on the USU campus using a legacy propulsion systems test cell that has been retrofitted for rocket motor testing. The propulsion test facilities used for this project will leverage prior USU hardware development activities. This existing hardware will form the basis of the test facility for developing and evaluating the proposed hybrid motor configurations. To date, more than 65 hybrid and 15 solid rocket motor tests have been performed in this test facility.

The test cell is fully instrumented and has expansion capability necessary to support all phases of this characterization testing. Available measurements obtained include chamber pressure, 6-degree of freedom (6-DOF) thrust, total impulse, motor case temperatures, exhaust plume temperatures, specific impulse, mass flow rate, consumed propellant mass, and propellant regression rate. Figure 7.1 shows a 98mm diameter motor mounted on the test cart.

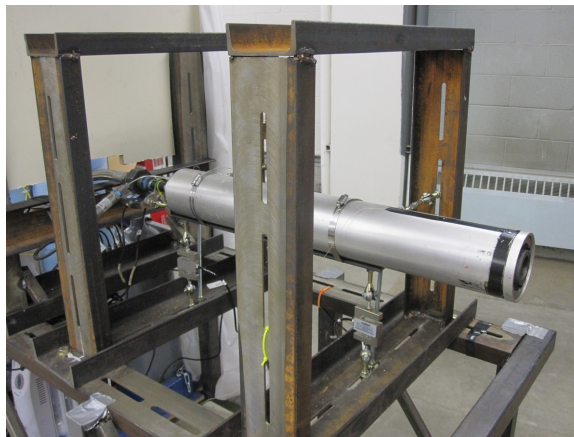


Fig. 7.1: Motor test stand with 98mm motor.

The test cell has been specially adapted for hybrid rocket testing. Figure 7.2 shows a piping and instrumentation diagram (P&ID) for the Mobile Nitrous Oxide Supply and Testing Resource (MoNSTeR) cart oxidizer delivery system. To allow sufficient mass flow rates with minimal line losses, a predetermined mass of N<sub>2</sub>O Oxidizer is delivered to a closely coupled run tank from a series of K sized industrial pressure cylinders. The helium top pressure is set by a manual regulator, and is typically maintained near 5200 kPa (800 psi) for these tests. The top pressure keeps the N<sub>2</sub>O above saturation pressure for the entire run and insures a single-phase liquid flow through the injector. The pneumatic run valve is triggered by an electronic relay and is automatically controlled by the instrumentation software. Oxidizer mass flow is sensed by vertical load cells mounted on the run tank and by an inline venturi flow meter mounted in the oxidizer feed-line just ahead of the injector.

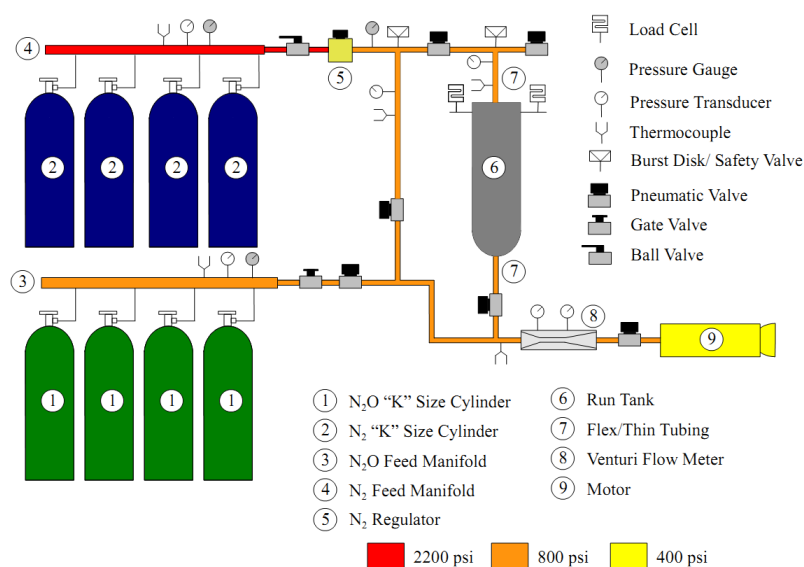


Fig. 7.2: MoNSTeR cart plumbing diagram.

Two National Instruments data acquisition and control devices manage motor fire control, and log test data. An NI-compact DAQ 4-slot bus controller with multiple analog input (16-bit), analog output, digital output, and thermocouple modules (24-bit) bus-cards manage the majority of the measurements and valve control. The digital outputs from a separate NI USB-6009 module are used to trigger the relays that fire the igniter e-matches.

Operators and experimenters are remotely located in a secure control room separated from the test area. Communications to the test stand are managed by an operator-controlled laptop via universal serial bus (USB) using amplified extension cables. All control and measurement functions are controlled by a LABview program hosted on the control laptop.

For testing rapid prototyped fuel grains, a 75mm diameter Cesaroni Pro75 [56] motor case was used, with in-house manufactured nozzle holder, injector, and nozzle. Figure 7.3 shows a section view of an assembled motor with a 12" long fuel grain.

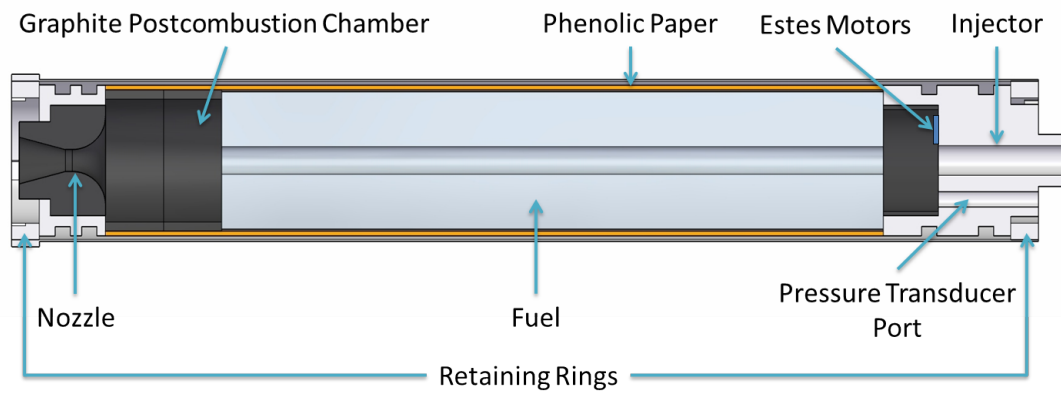


Fig. 7.3: Assembled fuel grain diagram.

For the validation of the geometric propagation model, several different fuel grain geometries must be burned. Initially, a maltese cross was decided upon as a benchmark fuel grain. This fuel grain has been burned before, and has a relatively simple parametric solution. The second fuel grain was designed to be four fuel grain geometries in one to reduce the number of burns required to test out different geometries. This fuel grain was nicknamed the “goldfish” fuel grain. Figure 7.4 shows the “goldfish” fuel grain and its four different grain geometries.

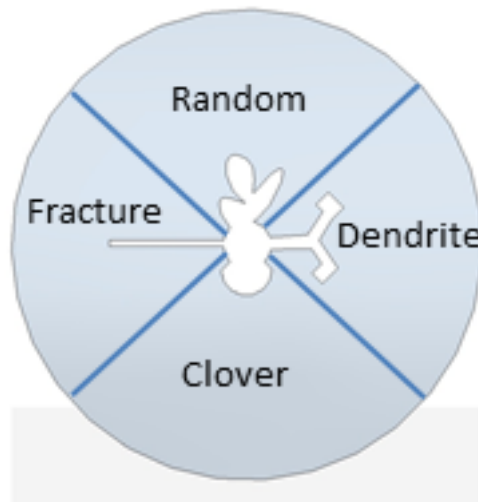


Fig. 7.4: Goldfish fuel grain

Initially the maltese cross and goldfish fuel grains were burned for two seconds. Following the initial burn, the fuel grains were removed from the motor for inspection and measurement. The fuel grains were weighed and regression measured by scanning a cross section of the grain. Both grains were then reinserted into the motor case and burned for another two seconds. It was decided for both fuel grains not to burn a 3rd or 4th time, as the maltese cross was coming very close to the outer edge of the fuel grain, and the goldfish fuel grain no longer had any unique geometry to be propagated.

Four helical fuel grains were burned. The burns consisted of two helix pitches, and two different injectors. All but the last helix fuel grain were burned for 3 seconds; the last helix fuel grain (large pitch, small injector) was burned for one second longer.

There are several possible metrics for comparison between the regression rate simulation and the burned fuel grains. The most obvious is a simple thrust comparison between model and experiment. This is compared, but the thrust data is relatively insensitive to small changes in grain geometry. A clearer method of comparison is to overlay the cross-sections of the burned fuel grain at the different burn times with that of the model. Before either comparison can be done, however, an estimate of the threshold amount must be found.

## 7.2 Threshold Characterization

While it may be possible to mathematically derive an appropriate value of the threshold value through heat transfer equations, the heat transfer that occurs within a hybrid fuel grain during a burn is extremely complex to model. It is relatively simple, however, to 'fit' a threshold value to a burned fuel grain, and then apply this threshold to future fuel grains. The cross-section of the 6" maltese cross was used for this. The cross section was analyzed in Matlab to determine the boundaries of the fuel after it had been burned. This data was loaded into the geometric regression simulation and plotted against the simulation results with the same area. The regression simulation then iterated through threshold values of  $n=0$  to  $N=0.5$ . Figure 6.4 shows a few of these iterations. From the plot, it is apparent that the desired threshold is between 0.3 and 0.4. Figure 7.6 shows a zoom in of this region. From this figure, the most accurate threshold value appears to be about  $n=0.36$ .

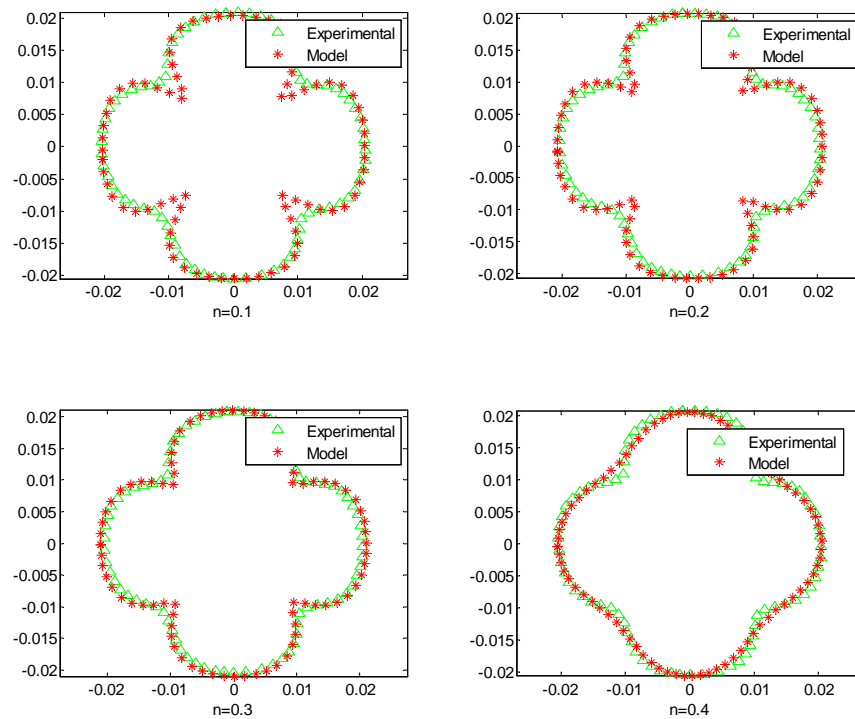


Fig. 7.5: Threshold matching



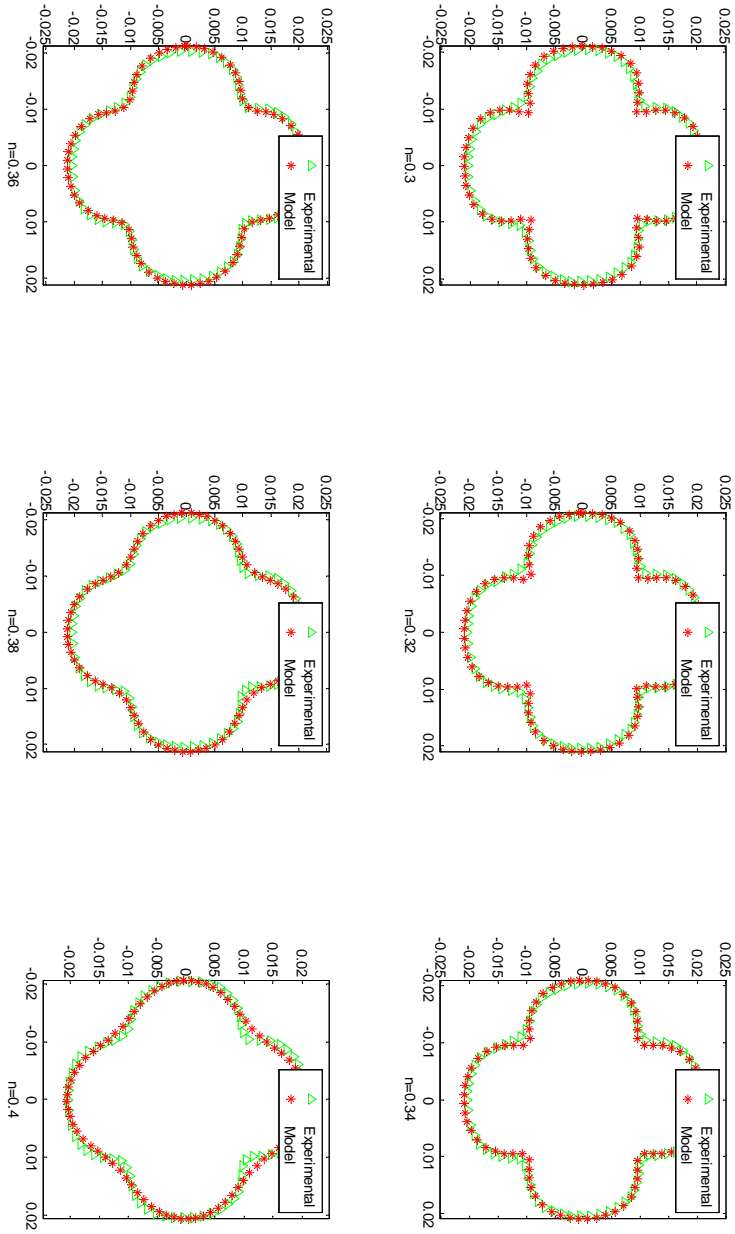


Fig. 7.6: Threshold matching zoom

### 7.3 Geometric Results Comparison

Using the chosen threshold value of  $n=0.36$ , the two geometries at both time steps were analyzed. This analysis is trivial for circular port fuel grains. The simulation outputs the exact same results as a parametric equation would (i.e.  $Surface\ Area = \pi DL$  and  $Volume = \pi r^2 L$ ). Figure 7.7 shows the results of the two fuel grain geometries.

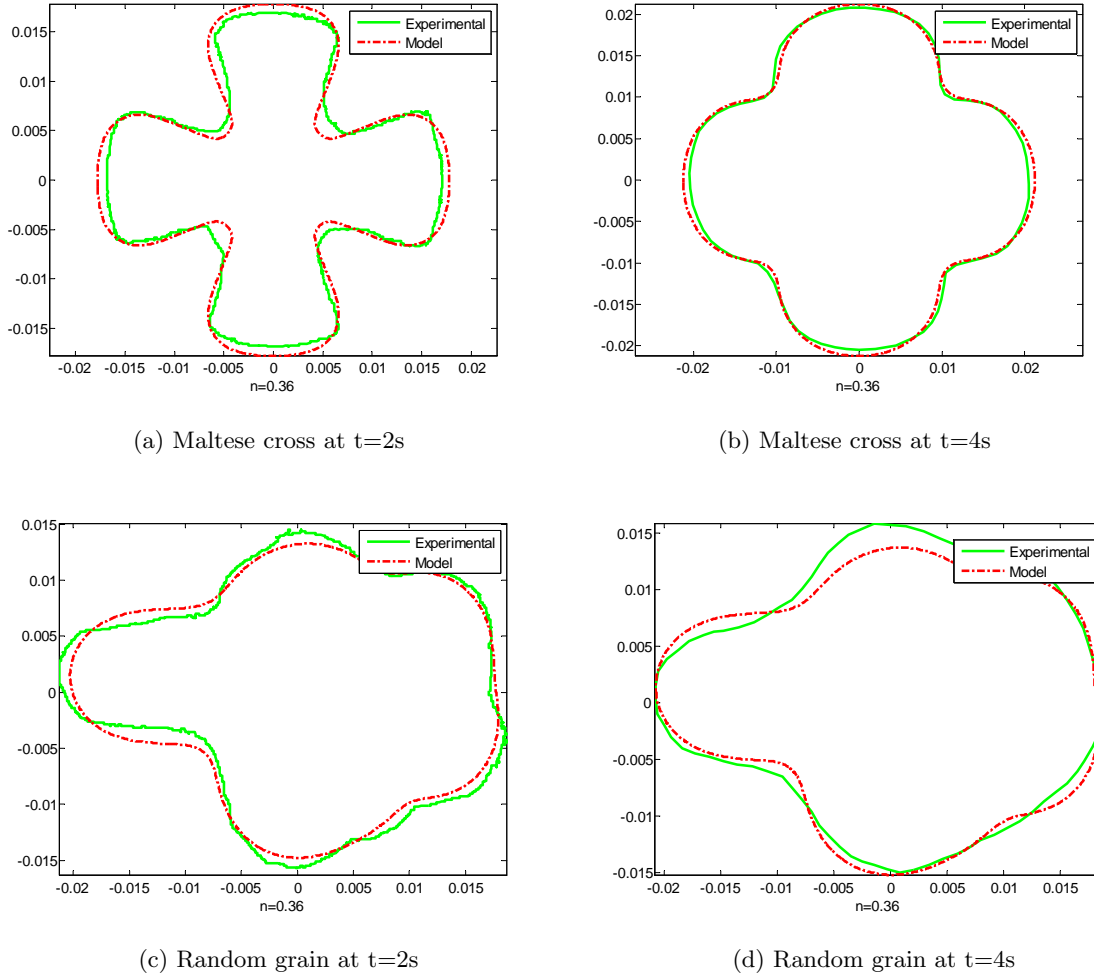


Fig. 7.7: Geometric propagator with thresholding vs. hot fire results summary

This solution works well for the Maltese cross grain, but not quite as well for the random geometry grain. For both grains, the  $t=2$  seconds cross section was one slice taken at approximately  $1/2$  of the distance from the injector end. For the  $t=4$  seconds cross section, both grains were cut into multiple sections, scanned, and then averaged longitudinally. This

is why the experimental lines for Figures 7.7b and 7.7d are much smoother than the other two.

The Maltese cross plots both match fairly well, with Figure 7.7b matching the best, as this was the case used to determine the threshold value. It does appear that for Figure 7.7a, the model does not work perfectly, but this is in part because it is not a longitudinally averaged cross section. Note that much of the model does not match the experimental because the burned cross section is asymmetric. When the asymmetries are ignored, the model appears to match the experimental cross section much better.

The 'goldfish' fuel grain cross sections did not match the model as well. This is in part because the fracture section, the section on the left, does not work well in the model. If the threshold value is high relative to the disk filter size, the fracture will not regress. The initial geometry was also complex enough that a small disk filter size had to be used to regress the grain, or else large parts of the fuel grain disappeared immediately, and the fracture section would also not regress. Ignoring the fracture section, Figure 7.7c matches quite well. Figure 7.7d does not match as well as the section at  $t=2$  seconds. This is because the second burn of this fuel grain exhibited a strange asymmetric burn. The bottom surface did not regress very much compared to the top surface. This is reflected in Figure 7.7d, as the model under-predicts the regression on the top surface.

It is also useful to see how the model does with no thresholding, as thresholding will still break down if the disk filter size becomes too small. Thresholding will conversely become computationally slow at large disk filter sizes, as the iterative solver to find a constant regression amount will find solutions on the order of 100's of pixels, which is an extremely large disk filter. Figure 7.8 shows the same plots as above, but with a  $n=0$  threshold.

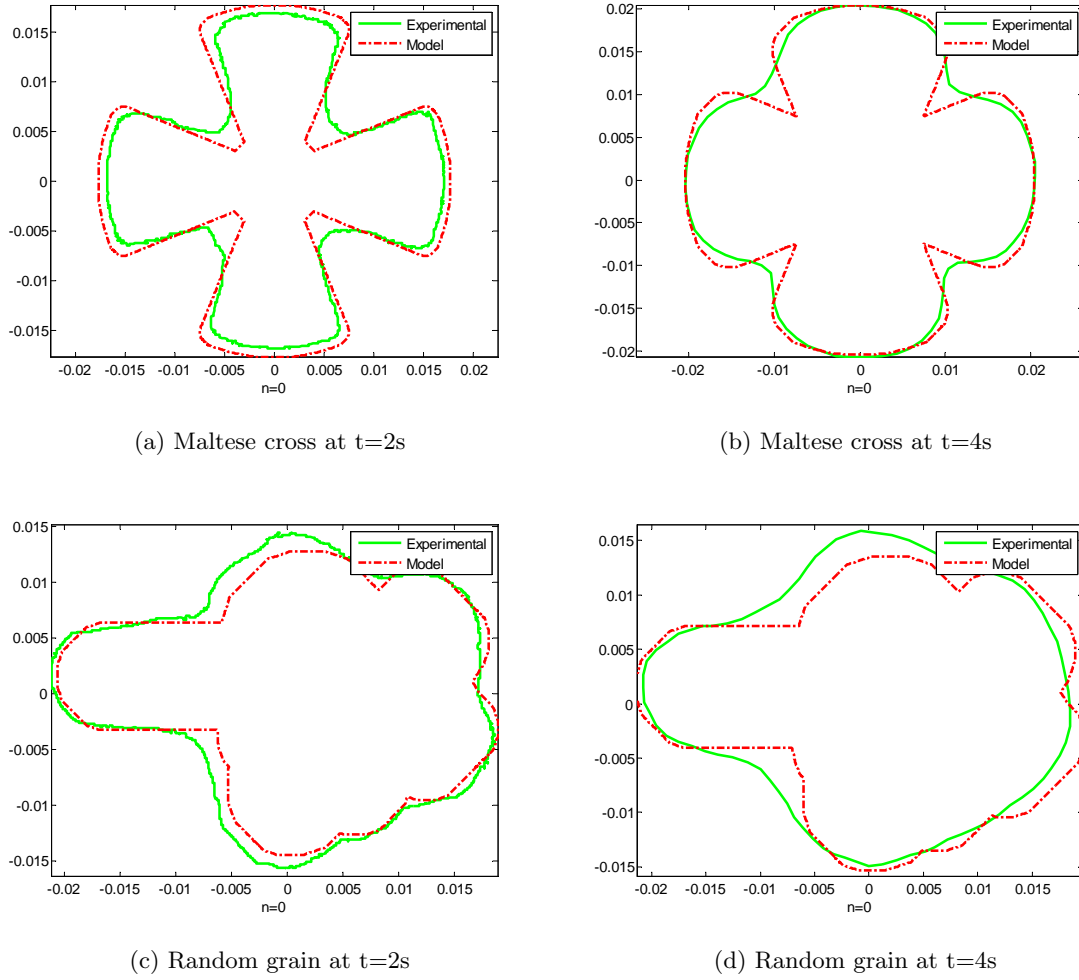


Fig. 7.8: Geometric propagator without thresholding vs. hot fire results summary

All four models match the results fairly well, with exception of the sharp edges predicted in the maltese cross burns. The second burn of the random grain is off again, because the fuel grain burned asymmetrically, as discussed in the paragraphs above.

It is helpful to know that this model is still relatively accurate with a zero threshold, making it more useful for applications that require fast computation time, such as thrust profile tailoring algorithms that may iterate through different fuel grain geometries hundreds or thousands of times.

This geometric propagation method does have some weaknesses. The goldfish fuel grain, for instance, does not regress well if the disk filter size is set too large when the

threshold value is set at 0.35. This is because the disk filter size that is solved for to obtain a constant regression rate at each time step is very large relative to the size of the geometry. Figure 7.9 illustrates this problem. The fracture section never regresses, and the small curves from the other geometric sections disappear as well.

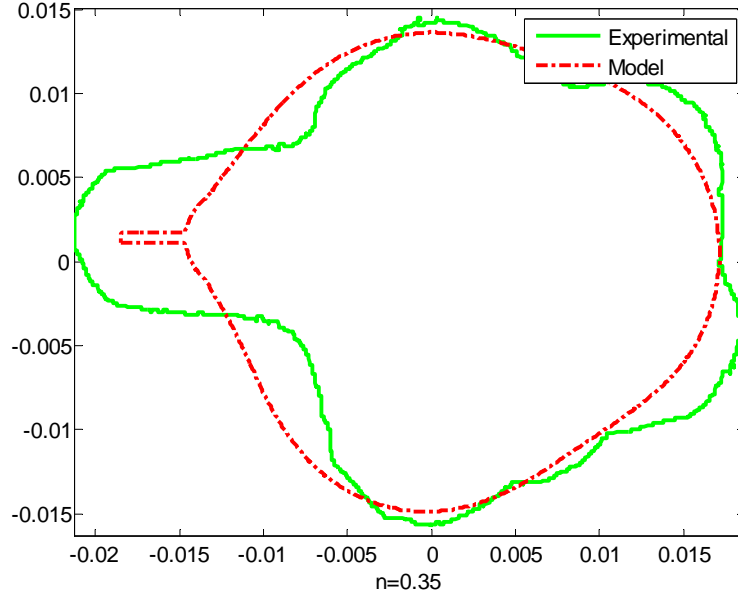


Fig. 7.9: Poor geometric propagation example

#### 7.4 Thrust Comparison

The geometric regression algorithm can be integrated into an end-to-end performance prediction routine for hybrid rockets, using the equations discussed in Section 4.2. To reduce run time, a lookup table of burning surface area and port volume for different burn depths was generated using the geometric regression simulation. This table can then be plugged into any existing hybrid burn model to predict burn performance. In this particular instance, the lookup table was implemented in a Simulink simulation developed by Spencer Chandler and Shannon Eilers, which uses the equations described in Section 4.2 and CEA lookup tables that give thermodynamic properties of ABS plastic. Figures 7.10 and 7.11 show both the simulated and actual burn data. The data from the hot-fire testing has been offset to remove start up transients. Note that the second 'goldfish' burn is again an outlier, as discussed

in the previous section. A second adjustment was done to the regression predictions. Note that in both fuel grains, the regression predicted is low, but with a small offset applied, the resulting line fits the measured data points extremely well. This is because the hybrid burn model used is less accurate at low O/F ratios, which is the case for both of these fuel grains. The average O/F for both of these fuel grains was on the order of 1.5. This accuracy reduction is because the regression equation used assumes that the fuel mass flow rate is small compared to the oxidizer mass flow, which clearly breaks down at low O/F ratios. This means that the G term in Equation 4.3 is actually much higher than calculated. This increases the net regression rate without significantly affecting thrust or chamber pressure.

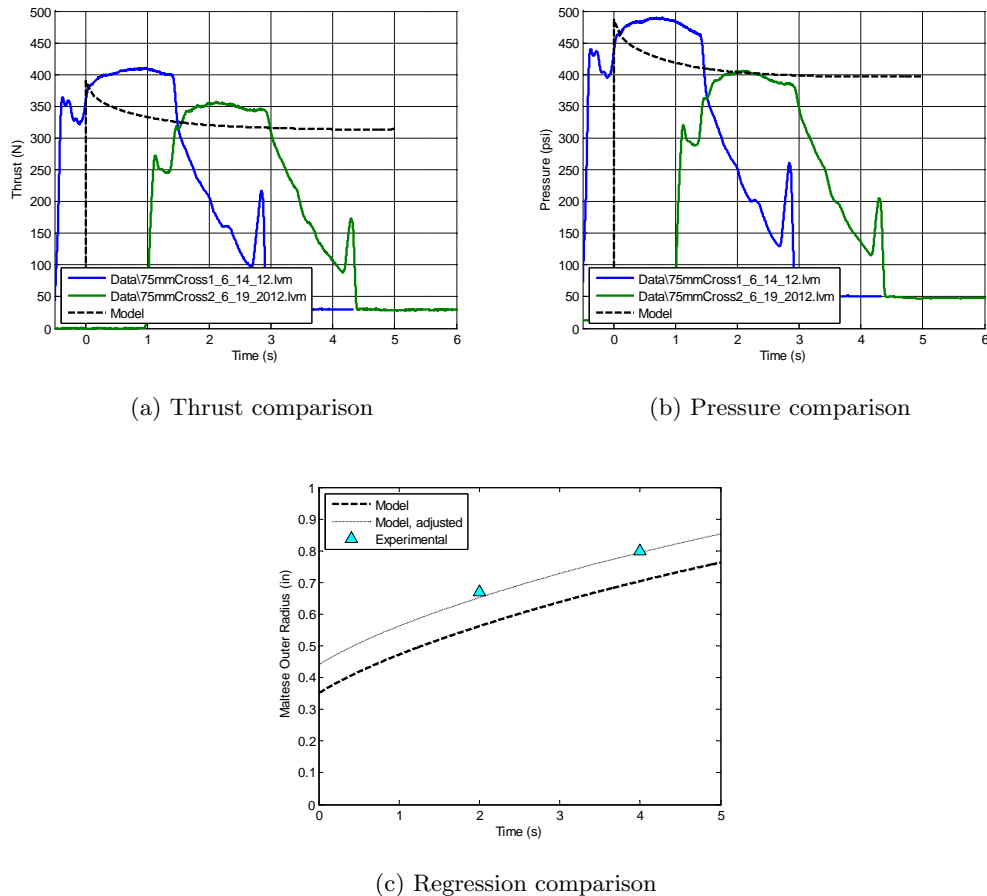


Fig. 7.10: Maltese cross performance comparison

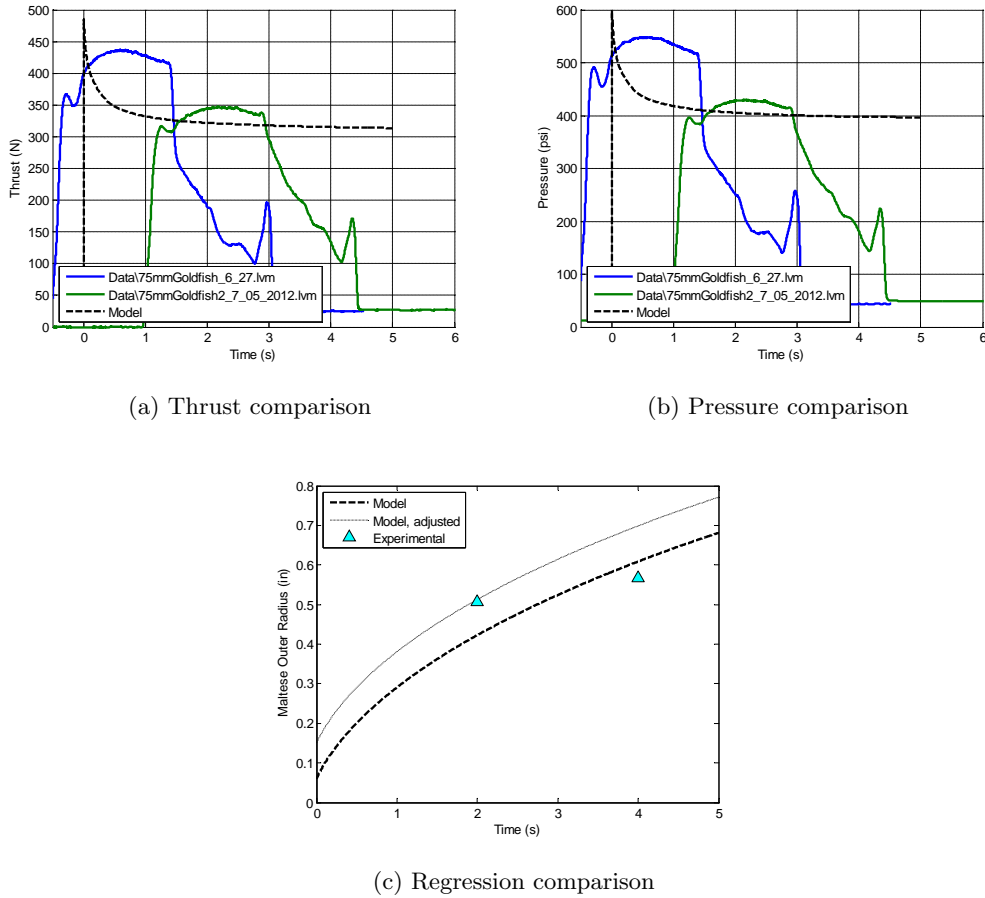


Fig. 7.11: Goldfish grain performance comparison

## 7.5 Helix Results

As an addition to this study, some preliminary helical fuel grains were designed and burned to learn more about their behavior. Helical fuel grains are only feasible to produce through rapid prototyping. They were first designed at USU with the idea to reduce the length of a fuel grain without changing the burning surface area. The first helical fuel grains burned showed a very large regression rate increase, making them of interest.

### 7.5.1 Data Analysis

After four helix burns, their behavior is still difficult to model. Even calculating the regression rate of a helix that has been burned is non-trivial. In order to extract an average

oxidizer mass flux and regression rate and from the helical fuel grains, they were weighed and then sliced into multiple 1/2" sections, painted white on the cuts to enhance contrast, and scanned into images. These images were then loaded into a Matlab image analysis code which scanned each image. The scan detected the outer radius of the fuel grain for scale conversion, and saved the inner boundary of the helical fuel grain slice. The code then created a triangular mesh between each boundary layer, stacking each layer vertically. The surface area  $A_{final}$  of the triangular mesh is then calculated. The average oxidizer mass flux of the burn is calculated by Eq. 7.1

$$G_{av} = \frac{\dot{m}_{ox}}{\pi r_{avg}^2} \quad (7.1)$$

Where  $\dot{m}_{ox}$  is the average oxidizer mass flux, from test data, and  $r_{avg}$  is the average diameter of a circle of equivalent area of a helical slice, calculated by Eq. 7.2

$$r_{avg} = \frac{r_{init} + r_{final}}{2} = \frac{\frac{2A_{init}}{P_{init}} + \frac{A_{final}}{\pi S}}{2} \quad (7.2)$$

Where the  $r_{init}$  term is calculated using effective hydraulic diameter, and  $r_{final}$  is calculated by assuming the surface area is that of a tube of length  $S$ , the total arc length of the helix. This assumption, while required to obtain a true regression rate metric, becomes a large issue. By the end of some of the burns, the fuel grain is no longer a helix, and therefore the arc length of the helix no longer applies.

In order to get the regression rate, the change in mass of the fuel grain was used to calculate a change in volume of an equivalent circular grain, as shown in Eq. 7.3

$$\dot{r}_{avg} = \frac{\Delta r}{t_{burn}} = \frac{\Delta V}{t_{burn} \frac{(A_{init} + A_{final})}{2}} = \frac{2\Delta m}{\rho_{fuel}(A_{init} + A_{final})t_{burn}} \quad (7.3)$$

Where  $\Delta r$  is the effective change in radius of an equivalent circular, straight port fuel grain, which is calculated by the change in volume,  $\Delta V$ , over the average burning surface area. The change in volume is calculated by the change in mass  $\Delta m$ , and density of the fuel  $\rho_{fuel}$ .



The primary source of regression rate enhancement in helix fuel grains is the increase in skin friction. This becomes obvious when observing the thrust and pressure plots of the helix burns, as shown in Figure 7.12. In a typical burn, thrust and pressure are very correlated. In a helix burn, the pressure spikes at the beginning of the burn, but the thrust does not. This de-correlation is essentially a pressure loss due to friction. Note also that by the end of the burn, the pressure is again correlated with the thrust. This is because much of the helix has burned out, and the pressure loss due to the helix becomes small.

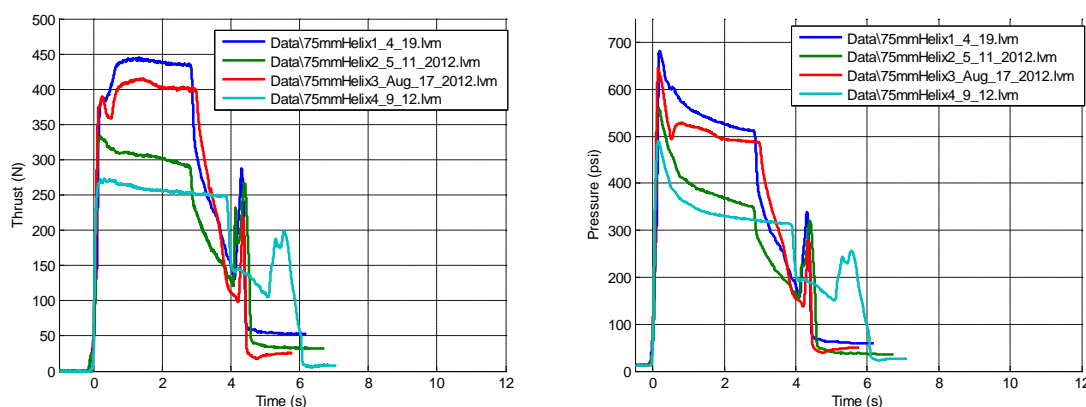


Fig. 7.12: Helix thrust and chamber pressure

As noted in the literature survey, there have been multiple studies on the increase in skin friction for helical tubes. There are also several other possible regression enhancing effects occurring in the helical fuel grain as it burns, such as a changing balance of centrifugal forces and diffusion, changing boundary layer thicknesses, and a changing balance of radiative and convective heat transfer. All of these are extremely difficult to model and predict, and would require at least an entire thesis, if not dissertation. For the sake of simplicity, only the effect of increased skin friction is predicted and results compared. It is difficult to find a skin friction equation that is valid for the Reynolds number regime the fuel grain experiences (around  $2e5$ ), especially for non-fully developed flow. In fact, all of the friction correlations are for fully-developed flow. Still, they can give a good order-of-magnitude estimate of the friction enhancement of the helix. The most recent friction correlation is by Gnielinski, given by Eq. 7.4

$$f_{c_{gniel}} = 0.0791Re^{-0.25} + 0.0075 \left( \frac{d}{D} \right)^{0.5} \quad Re_{cr} < Re < 1 \cdot 10^5 \quad (7.4)$$

Where  $d$  is the inner diameter of the helical tube, and  $D$  is the diameter of the helix. Note that this is also slightly outside the Reynolds number regime that the helix fuel grains experience, but it will still give some idea of magnitude. The friction of a straight port, circular fuel grain is calculated by the Blasius skin friction, shown in Eq. 7.5

$$f_{c_{blas}} = \frac{0.3164}{4Re^{0.25}} \quad (7.5)$$

The factor of increase in skin friction is then given by Eq. 7.6

$$F = \frac{f_{c_{gniel}}}{f_{c_{blas}}} \quad (7.6)$$

This friction increase is extremely important to hybrid regression. An alternate expression of the regression rate equation (Eq. 4.3) is given by Eq. 7.7

$$\dot{r} = \frac{0.635}{P_r^{0.1532}} \left( \frac{\Delta h_{flame\ surface}}{h_v} \right)^{0.23} \left( \frac{\rho_e U_e}{\rho_{fuel}} \right) C_f \quad (7.7)$$

The most important part to note in this equation is the friction coefficient,  $C_f$ , is directly proportional. Therefore a helical regression rate equation can be given as

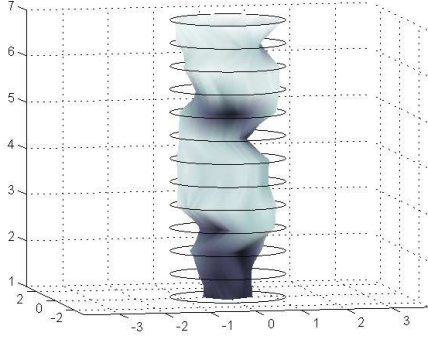
$$\dot{r}_{helix} = F\dot{r}. \quad (7.8)$$

This means that a simple method of predicting helical regression rate is to simply model the regression rate of a circular, straight port fuel grain, and multiply it by this friction factor.

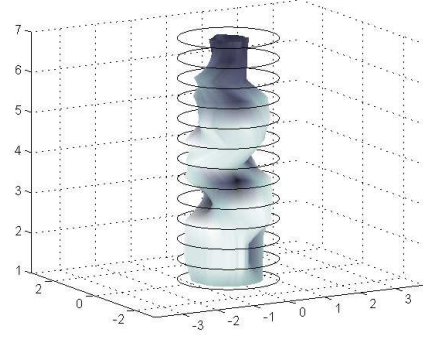
### 7.5.2 Helix Data

With the fuel grains analyzed for the oxidizer mass flux and regression rate, their performance can be compared to normal, straight port fuel grains. Figure 7.13 shows the

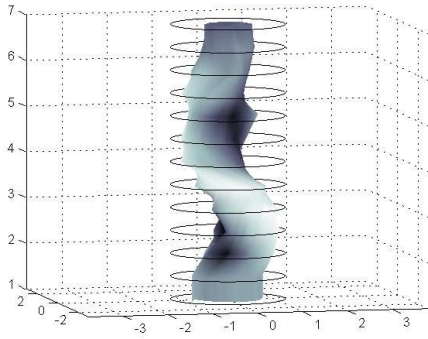
3D reproduction of each helix fuel grain after the burn.



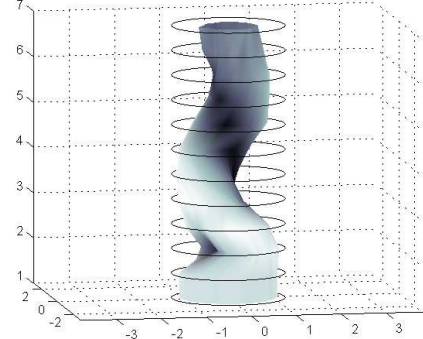
(a) Helix 1 (2.35in pitch, 0.10in injector)



(b) Helix 2 (2.35in pitch, 0.08in injector)



(c) Helix 3 (4.7in pitch, 0.10in injector)



(d) Helix 4 (4.7in pitch, 0.08in injector)

Fig. 7.13: Helix fuel grain 3D scans

The best metric to compare the performance increase of helix fuel grains is to compare the regression rate vs. oxidizer mass flux curves. Figure 7.14 shows the analytical and experimental curves for the standard 98mm, 75mm, and helical burns. The friction factor correction curve was created by calculating the friction factor from Equation 7.8, and multiplying the 75mm analytical curve by that factor. The friction factor calculated was 2.52 for a Reynolds number of  $2.5 \times 10^5$ , which was output by the hybrid simulation described in Section 7.4 with a modified Reynolds number calculation for a helical fuel grain.

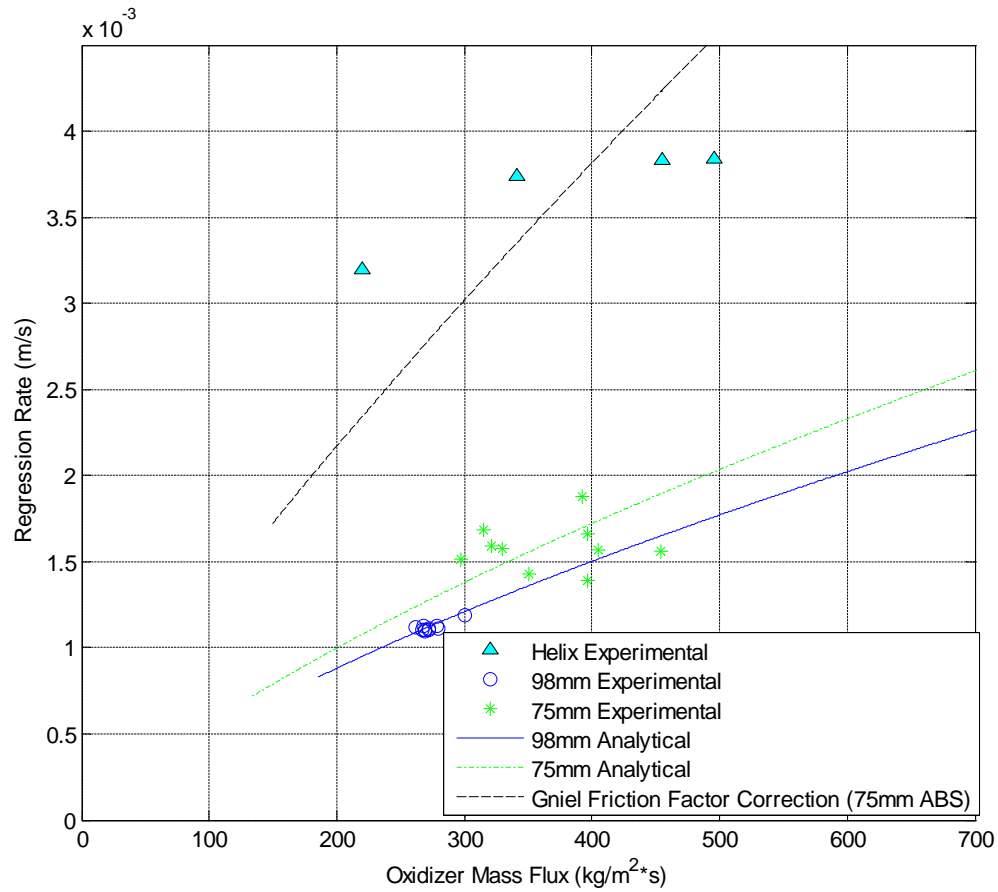


Fig. 7.14: Helical, 98mm, and 75mm regression rates

The most important thing to note is that all of the helix burns have a very significant increase in regression rate for the same range of oxidizer mass flux. The friction factor correction also does a good job in predicting the regression rate, although the slope is not very accurate. In part this is because as oxidizer mass flux changes, so does Reynolds number, but the friction factor correction was only calculated at one Reynolds number. Additionally, other phenomena occur in helix burns that are not significant in circular, straight port burns that are not taken into account by merely applying a friction factor to the 75mm curve.

## 7.6 Data Table

Table 7.1 summarizes the results from all hot-fire testing. Note that the fuel burned in the second “goldfish” burn is much lower than the first. This again shows it to be an outlier burn. The regression rate for the maltese grain was taken as an average over both burns. For the “goldfish” grain, the regression rate is for the first burn only. For the helix burns, the regression rate is calculated using Equation 7.2 in Matlab. Since the helix grains are still not well understood and not being investigated in depth for this study, only one friction coefficient was calculated and used, as it fits all four helix burns moderately well.

Table 7.1: Test plan matrix.

| Motor Test    | Burn Time (s) | Injector Diameter (in) | Helix Pitch (in) | Fuel Burned (g) | Friction Coefficient | Regression Rate (mm/s) |
|---------------|---------------|------------------------|------------------|-----------------|----------------------|------------------------|
| Maltese Cross | 2-2           | 0.10"                  | N/A              | 82/83           | N/A                  | 2.10                   |
| 'Goldfish'    | 2-2           | 0.10"                  | N/A              | 87/54           | N/A                  | 1.90                   |
| Helix 1       | 3             | 0.10"                  | 2.35"            | 203             | 2.52                 | 3.84                   |
| Helix 2       | 3             | 0.08"                  | 2.35"            | 198             | 2.52                 | 3.74                   |
| Helix 3       | 3             | 0.10"                  | 4.70"            | 152             | 2.52                 | 3.83                   |
| Helix 4       | 4             | 0.08"                  | 4.70"            | 152             | 2.52                 | 3.20                   |

## Chapter 8

### Summary and Conclusion

The purpose of this study was to investigate a new method of geometric propagation of complex fuel grain geometries, as well as preliminary investigations of helical fuel grains. Both parts of this were successful.

The geometric propagation algorithm does predict regression of fuel grains as arbitrarily shaped as the 'goldfish' grain, with exception of the fracture section, which behaves differently than most fuel geometries. This method can be adjusted to perform faster, as it does do a relatively good job of prediction even with a threshold value of 0. With a threshold value of 0, the simulation completes in 10's of seconds. This method works for a grain as simple as a maltese cross, but will also work for a complex, multi-port fuel grain. This capability to model any complex geometry fuel grain allows for any printable fuel grain to be quickly analyzed for its performance. It is also fast enough for performance tuning software to iterate through hundreds of different grain geometries in a matter of several minutes, such that custom optimized fuel grains are possible to be designed, produced, and fired in a matter of days rather than weeks.

This model does still have weaknesses. If a non-zero threshold value is used for the propagation, it slows down a significant amount. This brings the simulation time to the order of 60 seconds or more, compared to parametric methods which propagate a fuel grain in seconds. Additionally, while this method compensates for changing disk filter size with the threshold solver, solutions are still somewhat sensitive to disk filter size relative to the size of the picture, and the size of fuel grain geometry. If there are features smaller than the disk filter size, they will disappear completely in one iteration. If the disk filter size is too large or too small relative to the pixel size of the picture, the solutions become inaccurate.

Helical fuel grains need more investigation to be well understood, but preliminary

results suggest that helix fuel grains obtain a huge regression rate increase from skin friction amplification. This skin friction increase enhances heat transfer, which causes the fuel grain to regress faster. There are still, however, other phenomena that occur in helix fuel grains that would not occur in a straight-port fuel grain, and further research should be done in the subject.



## References

- [1] Whitmore, S. A., Peterson, Z. W., and Eilers, S. D., “Analytical and Experimental Comparisons of HTPB and ABS as Hybrid Rocket Fuels,” *47th AIAA/ASME/SAE/ASEE Joint Propulsion Conference & Exhibit*, 2011.
- [2] Lesage, A., “Solid Propellant Grain Geometry Design, a Model for the Evolution of Star Shaped Interfaces,” *Bachelor Project Report, Physics and Astronomy*, Vol. 12, 2010.
- [3] Wright, P. K., *21st Century Manufacturing*, Prentice-Hall Inc., Upper Saddle River, NJ, 2001.
- [4] Feldman, J., “Plastics - Materials of the 21st Century,” *BASF News Releases*, 2011.
- [5] Fuller, J., Ehrlich, D., Lu, P., Jansen, R., and Hoffman, J., “Advantages of Rapid Prototyping for Hybrid Rocket Motor Fuel Grain Fabrication,” *47th AIAA/ASME/SAE/ASEE Joint Propulsion Conference*, 2011.
- [6] Anon., “Hazard Analysis of Commercial Space Transportation; Vol. 1: Operations, Vol. 2: Hazards, Vol. 3: Risk Analysis,” *U.S. DOT, PB93-199040, Accession No. 00620693*, 1988.
- [7] Peterson, Z., Eilers, S. D., and Whitmore, S., “Closed-Loop Thrust and Pressure Profile Throttling of a Nitrous-Oxide HTPB Hybrid Rocket Motor,” *AIAA 2012-4551*, 2012.
- [8] G.A. Marxman, C. W. and Muzzy, R., “Fundamentals of Hybrid Boundary Layer Combustion,” *AIAA Heterogeneous Combustion Conference*, 1963.
- [9] Karabeyoglu, A., Stevens, J., and Cantwell, B., “Investigation of Feed System Coupled Low Frequency Combustion Instabilities in Hybrid Rockets,” *AIAA 2007-5366*, 2007.
- [10] Altman, D., “Hybrid Rocket Development History,” *27th AIAA, SAE, ASME, and ASEE, Joint Propulsion Conference*, 1991.
- [11] Galfetti, L., Merotto, L., Biocchi, F., Maggi, F., and De Luca, L., “Ballistic and Rheological Characterization of Paraffin-Based Fuels for Hybrid Rocket Propulsion,” *47th AIAA/ASME/SAE/ASEE Joint Propulsion Conference*, 2011.
- [12] Brandenburg, J. and Elzooghby, M., “Ethanol Gel Based Fuel for Hybrid Rockets: The Golden Knight Hybrid Rocket Program at the University of Central Florida,” *AIAA 2007-5361*, 2007.
- [13] Doran, E., Dyer, J., Lohner, K., Dunn, Z., Cantwell, B., and Zilliac, G., “Nitrous Oxide Hybrid Rocket Motor Fuel Regression Rate Characterization,” *AIAA 2007-5352*, 2007.
- [14] Pfeffer, D., *Lard Used as Fuel for Hybrid Rocket Motors*, Master’s thesis, University of Tennessee, Knoxville, 2007.

- [15] Chepko, A. B. and Droppers, L. J., "Characterization of a Hydrogen Peroxide and HTPB Hybrid Rocket Engine," *AIAA*, 2004.
- [16] Heister, S. D., Wernimont, E. J., and Rusek, J., "High Test Peroxide Hybrid Rocket Research," Tech. rep., 1998.
- [17] Lips, H. R., "Metal Combustion in High Performance Hybrid Rocket Propulsion Systems," *AIAA 1976-640*, 1976.
- [18] Farbar, E., Louwers, J., and Kaya, T., "Investigation of Metallized and Nonmetallized Hydroxyl Terminated Polybutadiene/Hydrogen Peroxide Hybrid Rockets," *Journal of Propulsion and Power*, Vol. 23, 2007, pp. 476–486.
- [19] Chiaverini, M. J., Serin, N., Johnson, D. K., Lu, Y.-C., Kuo, K. K., and Risha, G. A., "Regression Rate Behavior of Hybrid Rocket Solid Fuels," *Journal Of Propulsion and Power*, Vol. 16, 2000.
- [20] Evans, B., Favorito, N. A., and Kuo, K. K., "Oxidizer-Type and Aluminum-Particle Addition Effects on Solid-Fuel Burning Behavior," *42nd AIAA/ASME/SAE/ASEE Joint Propulsion Conference*, 2006.
- [21] George, P., Krishnan, S., Varkey, P. M., Ravindran, M., and Ramachandran, L., "Fuel Regression Rate in Hydroxyl-Terminated-Polybutadiene/ Gaseous-Oxygen Hybrid Rocket Motors," *JOURNAL OF PROPULSION AND POWER*, Vol. 17, 2001.
- [22] Marothiya, G., Kumar, R., and P.A., R., "Enhancement of Regression Rate in Hybrid Rockets," *47th AIAA/ASME/SAE/ASEE Joint Propulsion Conference*, 2011.
- [23] Larson, D., Boyer, E., Wachs, T., and Kuo, K., "Characterization of the Performance of Paraffin / LiAlH<sub>4</sub> Solid Fuels in a Hybrid Rocket System," *47th AIAA/ASME/SAE/ASEE Joint Propulsion Conference*, 2011.
- [24] Evans, B., Boyer, E., Kuo, K. K., Risha, G., and Chiaverini, M., "Hybrid Rocket Investigations at Penn State University's High Pressure Combustion Laboratory: Overview and Recent Results," *AIAA 2009-5349*, 2009.
- [25] Boronowsky, K., *Non-homogeneous Hybrid Rocket Fuel for Enhanced Regression Rates Utilizing Partial Entrainment*, Master's thesis, San Jose State University, 2011.
- [26] Arves, J. P., Jones, H. S., Kline, K., Smith, K., Slack, T., and Bales, T., "Development of a N<sub>2</sub>O/HTPB Hybrid Rocket Motor," *AIAA 1997-2803*, 1997.
- [27] Dyer, J., Doran, E., Dunn, Z., Lohner, K., Bayart, C., Sadhwani, A., Zilliac, G., Cantwell, P. B., and Karabeyoglu, A., "Design and Development of a 100 km Nitrous Oxide/Paraffin Hybrid Rocket Vehicle," *AIAA 2007-5362*, 2007.
- [28] Karabeyoglu, A., Zilliac, G., Cantwell, B., Dezilwa, S., and Castellucci, P., "Scale-up Tests of High Regression Rate Paraffin-Based Hybrid Rocket Fuels," *Journal of Propulsion and Power*, Vol. 20, 2004, pp. 1037–1045.

- [29] Sutton, G. P. and Biblarz, O., *Rocket Propulsion Elements Seventh Edition*, Wiley, 2001.
- [30] Smiley, M., Veno, M., and Bell, R., “Commercial Crew Development - Round One, Milestone 3: Overview of Sierra Nevada Corporation’s Hybrid Motor Ground Test,” *47th AIAA/ASME/SAE/ASEE Joint Propulsion Conference*, 2011.
- [31] Thompson, R. J., “Research in Hybrid Combustion Rocketdyne Summary Rept. R-2267,” Tech. rep., Rocketdyne, 1963.
- [32] Eilers, S. D. and Whitmore, S. A., “Correlation of Hybrid Rocket Propellant Regression Measurements with Enthalpy-Balance Model Predictions,” *AIAA 2007-5349*, 2007.
- [33] Marxman, G. and M. Gilbert, “Turbulent Boundary Layer Combustion in the Hybrid Rocket,” *Symposium (International) on Combustion*, Vol. 9, 1963, pp. 371–383.
- [34] Strand, L. D., Ray, R. L., Anderson, F. A., and Cohen, N. S., “Hybrid Rocket Combustion Study,” *AIAA Paper 93-2412*, 1993.
- [35] Chiaverini, M. J., Kuo, K. K., Peretz, A., and Harting, G. C., “Regression-rate and Heat-transfer Correlations for Hybrid Rocket Combustion,” *Journal of Propulsion and Power*, Vol. 17, 2001.
- [36] Estey, P., Altman, D., and McFarlane, J., “An Evaluation of Scaling Effects for Hybrid Rocket Motors,” *AIAA-91-2517*, 1991.
- [37] Whitmore, S. A. and Chandler, S., “An Engineering Model for Saturated N<sub>2</sub>O Propellant Feed Systems,” *AIAA Journal of Propulsion and Power*, Vol. 26, 2010, pp. 706–714.
- [38] Karabeyoglu, M. A., Cantwell, B. J., and Zilliac, G., “Development of Scalable Space-time Averaged Regression Rate Expressions for Hybrid Rockets,” *41st AIAA/ASME/ASEE Joint Propulsion Conference, Tucson AZ*, 2005.
- [39] Dean, W., “XVI. Note on the Motion of Fluid in a Curved Pipe,” *Philosophical Magazine Series 7*, Vol. 4, No. 20, 1927, pp. 208–223.
- [40] Dean, W., “LXXII. The Stream-line Motion of Fluid in a Curved Pipe (Second paper),” *Philosophical Magazine Series 7*, Vol. 5, No. 30, 1928, pp. 673–695.
- [41] Mishra, P. and Gupta, S. N., “Momentum Transfer in Curved Pipes,” *Industrial & Engineering Chemistry Process Design and Development*, Vol. 18, 1979, pp. 130–137.
- [42] Havas, G., Deak, A., and Sawinsky, J., “Heat Transfer to Helical Coils in Agitated Vessels,” *The Chemical Engineering Journal*, Vol. 35, 1987, pp. 61–64.
- [43] Yang, R. and Chiang, F. P., “An Experimental Heat Transfer Study for Periodically Varying-curvature Curved-pipe,” *International Journal of Heat and Mass Transfer*, Vol. 45, October 2001, pp. 3199–3204.

- [44] Hartfield, R., Jenkins, R., Burkhalter, J., and Foster, W., “A Review of Analytical Methods for Solid Rocket Motor Grain Analysis,” *39th Joint Propulsion Conference and Exhibit*, 2003.
- [45] Ricciardi, A., “Complete Geometric Analysis of Cylindrical Star Grains,” *25th AIAA/ASME/SAE/ASEE Joint Propulsion Conference*, 1989.
- [46] Zarda, P. R., Hartman, D. J., and Group, M. M. E. . M., “Computer-Aided Propulsion Burn Analysis,” *24th AIAA/ASME/SAE/ASEE Joint Propulsion Conference*, 1988.
- [47] Sethian, J. A., “Numerical Algorithms for Propagating Interfaces: Hamilton-Jacobi Equations and Conservation Laws,” *Journal of Differential Geometry*, Vol. 31, 1990, pp. 131–161.
- [48] Dauch, F. and Ribereau, D., “A Software for SRM Grain Design and Internal Ballistics Evaluation, PIBAL,” *38th AIAA/ASME/SAE/ASEE Joint Propulsion Conference*, 2002.
- [49] Favini, B., Cavallini, E., Giacinto, M. D., and Serraglia, F., “An Ignition-to-Burn Out Analysis of SRM Internal Ballistic and Performances,” *44th AIAA/ASME/SAE/ASEE Joint Propulsion Conference*, 2008.
- [50] Yildirim, C. and Aksel, M. H., “Numerical Simulation of the Grain Burnback in Solid Propellant Rocket Motor,” *41st AIAA/ASME/SAE/ASEE Joint Propulsion Conference*, 2005.
- [51] Willcox, M. A., Brewster, M. Q., Tang, K., and Stewart, D. S., “Solid Propellant Grain Design and Burnback Simulation using a Minimum Distance Function,” *41st AIAA/ASME/SAE/ASEE Joint Propulsion Conference*, 2005.
- [52] Hejl, R. J. and Heister, S. D., “Solid Rocket Motor Grain Burnback Analysis Using Adaptive Grids,” *Journal of Propulsion and Power*, Vol. 11, 1995, pp. 1006–1011.
- [53] Fang, S., Hu, K., Zhang, P., and Ma, Z., “A New Simulation Method for 3-D Propellant Grain Burn Analysis of Solid Rocket Motor,” *30th AIAA/ASME/SAE/ASEE Joint Propulsion Conference*, 1994.
- [54] Kamran, A. and Guozhu, L., “Design and Optimization of 3D Radial Slot Grain Configuration,” *Chinese Journal of Aeronautics*, Vol. 23, 2010, pp. 409–414.
- [55] Qazi, M. U., Masood, K., and Mahmood, K., “Rapid Prediction of Star Propellant Grain Regression using CAD Software,” *Proceedings of International Bhurban Conference on Applied Sciences & Technology*, 2009.
- [56] Pro75”, C., <http://pro38.com/products/pro75/pro75.php>, accessed September 2012.